The mechanism of shape instability for a vesicle in extensional flow

Vivek Narsimhan[1], **Andrew P. Spann**[2] **and Eric S. G. Shaqfeh**[1,2,3,†]

[1]Department of Chemical Engineering, Stanford University, Stanford, CA 94305, USA

[2]Institute of Computational and Mathematical Engineering, Stanford University, Stanford, CA 94305, USA

[3]Department of Mechanical Engineering, Stanford University, Stanford, CA 94305, USA

When a flexible vesicle is placed in an extensional flow (planar or uniaxial), it undergoes two unique sets of shape transitions that to the best of the authors' knowledge have not been observed for droplets. At intermediate reduced volumes (i.e. intermediate particle aspect ratio) and high extension rates, the vesicle stretches into an asymmetric dumbbell separated by a long, cylindrical thread. At low reduced volumes (i.e. high particle aspect ratio), the vesicle extends symmetrically without bound, in a manner similar to the breakup of liquid droplets. During this 'burst' phase, 'pearling' occasionally occurs, where the vesicle develops a series of periodic beads in its central neck. In this paper, we describe the physical mechanisms behind these seemingly unrelated instabilities by solving the Stokes flow equations around a single, fluid-filled particle whose interfacial dynamics is governed by a Helfrich energy (i.e. the membranes are inextensible with bending resistance). By examining the linear stability of the steady-state shapes, we determine that vesicles are destabilized by curvature changes on its interface, similar to the Rayleigh–Plateau phenomenon. This result suggests that the vesicle's initial geometry plays a large role in its shape transitions under tension. The stability criteria calculated by our simulations and scaling analyses agree well with available experiments. We hope that this work will lend insight into the stretching dynamics of other types of biological particles with nearly incompressible membranes, such as cells.

Key words: biological fluid dynamics, instability, low-Reynolds-number flows

---

1. Introduction and motivation

In the past 20 years, the biophysics community has demonstrated a keen interest in characterizing the response of biological particles to various types of mechanical forces. Vesicles, which are sacs of fluid enclosed by a lipid bilayer, are one example of such particles. These fluid sacs perform many important biological functions in living cells, such as the storage and transport of nutrients, as well as the control of osmotic pressure (Alberts *et al.* 2004). In biomedical applications, artificial vesicles

† Email address for correspondence: esgs@stanford.edu

(so-called liposomes) are common encapsulation agents for drug delivery with regard to cancer treatments (Sharma & Sharma 1997; Medina, Zhu & Kairemo 2004; Immordino, Dosio & Cattel 2006). In addition, liposomes have been of interest in areas ranging from self-assembly (Antonietti & Forster 2003) to miniature bioreactors (Noireaux & Libchaber 2004). Understanding the deformation of these particles under various forces provides useful knowledge for such applications, as well as insight into the dynamics of other biological particles characterized by soft, nearly incompressible membranes.

In this study, we will examine simple vesicles, which are unilamellar lipid membranes enclosing a Newtonian fluid. These particles are much simpler than eukaryotic cells, which have a non-Newtonian interior fluid, as well as a membrane with shear elasticity due to the presence of a cytoskeletal network. Nevertheless, certain aspects of cell deformation are similar to those of vesicles, and the basic physics of these motions can be explained through simple vesicle models. Examples of physics that can be explained through vesicle models include the biconcave shape of red blood cells, as well as the tank-treading/tumbling/swinging motions of these cells in shear flow (Abkarian & Viallat 2008; Vlahovska, Podgorski & Misbah 2009).

In the past decade, several authors have extensively studied the single- and multi-particle dynamics of simple vesicles in shear flow. Such studies include: (*a*) the characterization of vesicle tank treading/tumbling/swinging motion (Mader *et al.* 2006; Vlahovska & Gracia 2007; Dechamps, Kantsler & Steinberg 2009; Zhao & Shaqfeh 2011); (*b*) the induced hydrodynamic lift of a single vesicle near a wall (Callens *et al.* 2008; Podgorski *et al.* 2011; Zhao, Spann & Shaqfeh 2011); (*c*) pair interactions between two vesicles (Kantsler, Segre & Steinberg 2008*b*; Gires, Danker & Misbah 2012; Levant *et al.* 2012; Zhao & Shaqfeh 2013*a*); and (*d*) the measurement of the effective viscosity of a dilute vesicle suspension (Kantsler *et al.* 2008*b*; Vitkova *et al.* 2008). Recent studies also examine the role of membrane thermal fluctuations on the flow dynamics of vesicles (Zabusky *et al.* 2011; Levant & Steinberg 2012; Abreu & Seifert 2013). Despite the wealth of information of vesicles in shear flow, we are only aware of two experiments characterizing these particles in extensional flows, the details of which we describe below.

When a vesicle of high aspect ratio is placed in a planar extensional flow, it stretches to a steady-state shape at low extension rate, but appears to extend indefinitely in a symmetrical fashion above a critical extension rate (Kantsler, Segre & Steinberg 2008*a*). This behaviour is similar to the capillary breakup of droplets in such flows (Rallison 1984; Stone 1994), although the shapes in these two situations are qualitatively different. After the onset of continuous deformation, the vesicles have a much more dumbbell-like shape than the droplets, as well as a smaller central neck (figure 1*a*,*b*). As the deformation increases, the vesicles form pearls at the neck, which are 'bulges' with a size characteristic of the neck's radius (figure 1*b*). We emphasize that this pearling takes effect during flow, while such effects for droplets almost always occur after flow cessation, when the standard Rayleigh–Plateau instability takes place (Tomotika 1935; Stone, Bentley & Leal 1986). Kantsler *et al.* characterized the critical extension rates for these vesicle shape transitions, and they found that the transitions are sensitive to the initial (no-flow) geometry of the vesicle, particularly the vesicle's aspect ratio (Kantsler *et al.* 2008*a*). Unlike droplets, vesicles possess non-spherical initial shapes due to the mechanical properties of their lipid bilayers, which are nearly incompressible and cannot be described by a simple surface tension. Although current experiments on vesicles have not examined the dependence of the critical extension rate on the viscosity mismatch between the inner and outer fluids,
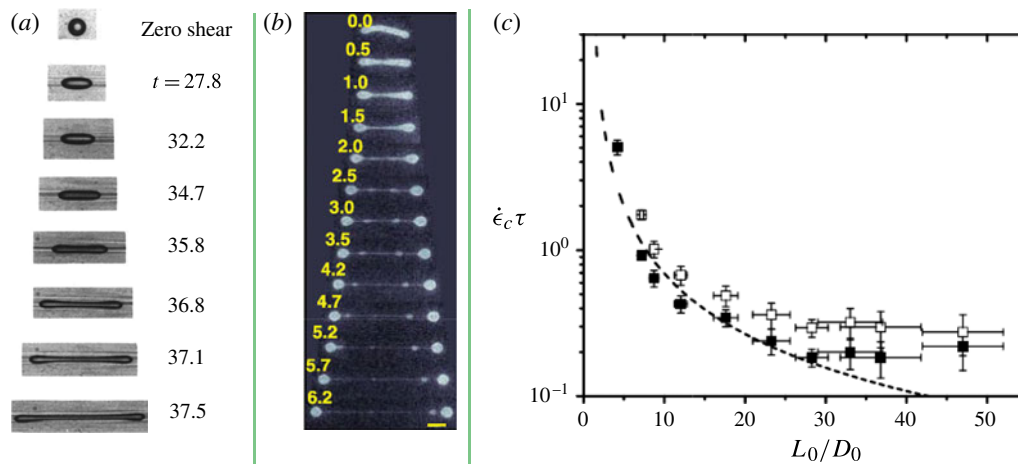
FIGURE 1. (Colour online) Comparison between droplets and high-aspect-ratio vesicles in planar extensional flows. (*a*) Droplet with viscosity ratio $\lambda = \mu_{in}/\mu_{out} = 2.4$, deforming at an extension rate of $\dot{\epsilon} = 0.132 \text{ s}^{-1}$. The pictures from top to bottom represent snapshots in time during continuous deformation (time is non-dimensionalized by $\dot{\epsilon}^{-1}$). (Reproduced with permission from Stone *et al.* (1986).) (*b*) A DOPC (dioleoyl-phosphatidylcholine) vesicle with initial aspect ratio 8.8 and matched viscosity ratio, deforming at an extension rate of $\dot{\epsilon} = 0.31 \text{ s}^{-1}$. The pictures from top to bottom represent snapshots in time during continuous deformation. The numbers are dimensionless time $t\dot{\epsilon}$, and the scale bar is 10 µm. (Reproduced with permission from Kantsler *et al.* (2008*a*).) (*c*) Stability boundary for a vesicle, as a function of the vesicle's initial aspect ratio. Black dots represent extension rates above which the vesicle deforms continuously, while the white dots represent extension rates above which pearls are observed. (Reproduced with permission from Kantsler *et al.* (2008*a*).)

we will later show that such a dependence is very weak, which is in strong contrast to the droplet case (see Bentley & Leal 1986; Stone 1994).

When the vesicle's aspect ratio is smaller (between three and six), its behaviour in planar extensional flow appears to be qualitatively different than that described above. Susan Muller (Spjut 2010) placed an intermediate-aspect-ratio vesicle in a four-roll mill, and when the extension rate increased above a critical value, the vesicle transitioned into an unsteady, *asymmetric* dumbbell separated by a long, cylindrical thread (figure 2*a*). Recent simulations by Zhao & Shaqfeh (2013*b*) observe this same phenomenon (figure 2*b*), and they quantify the conditions under which the vesicle becomes unstable (albeit, only for the case when fluids inside and outside the vesicle have matched viscosities). The asymmetric shape transition does not occur for droplets with a clean interface, although a few studies have observed this phenomenon when surfactants strongly adsorb onto the droplet, creating a nearly incompressible interface (Janssen, Boon & Agterof 1997; Hu, Pine & Leal 2000).

In this paper, we elucidate the major physics behind the extensional flow instabilities described in the previous two paragraphs. We solve the Stokes flow equations around a single vesicle, and determine the conditions under which this flow destabilizes perturbations to the vesicle's shape. In §2, we describe the constitutive model we use for the vesicle interface, as well as the numerical techniques we employ to solve the Stokes equations. Section 3 discusses our results in the intermediate-aspect-ratio limit,
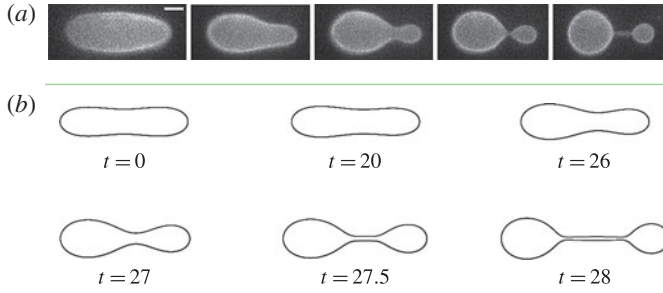
FIGURE 2. (Colour online) Intermediate-aspect-ratio vesicles in extensional flows. (*a*) Giant, unilamellar vesicle in planar extensional flow during instability. (Reproduced with permission from Spjut (2010).) The extension rate is $\dot{\epsilon} = 0.7$ s^{-1}, and the scale bar is 5 µm. The inner and outer fluid are viscosity matched. (*b*) Snapshots of the instability from boundary integral simulations (reduced volume = 0.65, capillary number = 10). (Reproduced with permission from Zhao & Shaqfeh (2013*b*).)

where the shape instability creates asymmetrical dumbbells. Section 4 states the results in the high-aspect-ratio limit, where symmetric burst and subsequent pearling occurs. We conclude our findings in §5, as well as discuss future directions for our work. *The central message from this study is that vesicles are destabilized by curvature changes at their interface, which can be described as a modified Rayleigh–Plateau instability.*

2. Model and numerical methods

2.1. *Equations and choice of constitutive model*

We show the geometry and set-up of the problem in figure 3. Suppose we subject a single vesicle to an extensional flow field:

$$\boldsymbol{u}^\infty = \dot{\epsilon}(z\hat{\boldsymbol{z}} + (\alpha - \tfrac{1}{2})y\hat{\boldsymbol{y}} + (-\alpha - \tfrac{1}{2})x\hat{\boldsymbol{x}}) \tag{2.1}$$

with the viscosities of the fluids interior and exterior to the vesicle being μ_{in} and μ_{out}. In the above equation, α is a parameter that controls what type of extensional flow the vesicle experiences. In most experiments, the flow field is a planar extensional flow ($\alpha = 1/2$). In our study, we will primarily examine uniaxial extensional flow ($\alpha = 0$), showing *a posteriori* that there is very little difference in the results between these two flow types (see §3.4, especially figure 13).

In the experiments described in the introduction (Kantsler *et al.* 2008*a*; Spjut 2010), the vesicles are typically of size $a \sim 10$ µm, and the extension rate is $\dot{\epsilon} \sim 1$ s^{-1}. In this case, the particle Reynolds number is $Re = \rho\dot{\epsilon}a^2/\mu_{out} \approx 10^{-4}$, and hence the flow around the particle is governed by the Stokes equations

$$\eta\nabla^2\boldsymbol{u} = \nabla p, \quad \nabla \cdot \boldsymbol{u} = 0 \tag{2.2a,b}$$

where $\boldsymbol{u}$ is the fluid velocity, p is the pressure, and η is the viscosity of the fluid (μ_{out} for the exterior of the particle and μ_{in} for the interior). We will neglect translational Brownian motion of the vesicle, since the Péclet number is $Pe = 6\pi\mu_{out}a^3\dot{\epsilon}/(kT) \approx 4500$. We will also neglect thermal fluctuations of the interface, although recent studies by Dechamps *et al.* (2009) suggest that such dynamics may be important in shear flow.
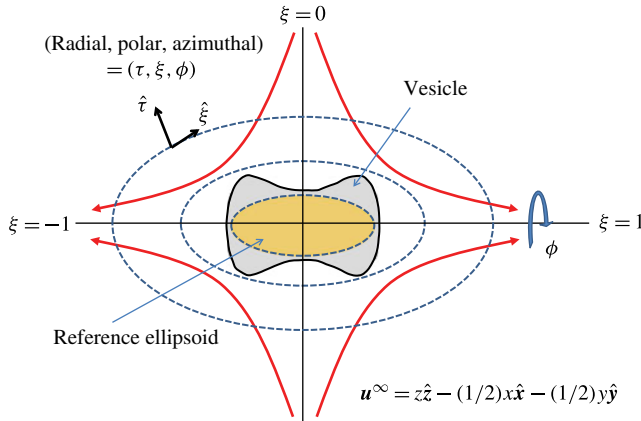
FIGURE 3. (Colour online) Geometry of a vesicle in spheroidal coordinates. In uniaxial extensional flow, the vesicle takes an axisymmetric geometry that can be described by prolate spheroidal coordinates. The coordinate system is characterized by the triad (τ, ξ, ϕ), where a surface of constant τ is a prolate spheroid. The variables $\theta = \cos^{-1}(\xi)$ and ϕ are the polar and azimuthal angles. Every spheroidal coordinate system also has a reference spheroid (shown in yellow online). We choose the reference spheroid to be reasonably close to the vesicle's geometry, so that the radial coordinate τ is nearly constant along the vesicle's interface. See (2.8) for conversion between Cartesian and spheroidal coordinates.

At mechanical equilibrium, the velocity field must be continuous across the particle's membrane, as well as satisfy a force balance on the interface. For droplets, the interfacial forces are surface tension, which leads to the standard result that the tangential stresses are continuous across the interface, while the normal stresses are discontinuous with a jump described by the capillary forces (Leal 2007). For a vesicle, the interface is a thin lipid bilayer that has bending resistance and strongly resists changes in local area (at least during the flow time scale $\dot{\epsilon}^{-1}$, which is the experimentally relevant one (Seifert 1997)). A popular model that takes these observations into account is the Helfrich model (Helfrich 1973), which states that the energy of the membrane consists of bending deformation and a constraint on local area:

$$E = \frac{\kappa}{2} \int (2H - c_0)^2 + \int \sigma \alpha \, \mathrm{d}A, \quad \text{where} \quad \alpha = (\mathrm{d}A - \mathrm{d}A_0)/\mathrm{d}A. \tag{2.3}$$

In the above equation, κ, H, c_0 and σ are the bending modulus, mean curvature, spontaneous curvature, and surface tension of the membrane. The surface tension is not a material parameter, but a spatially varying field that forces the local areal strain to be zero ($\alpha = 0$). This statement of membrane incompressibility is equivalent to setting the surface divergence of the velocity to be zero: $\nabla_s \cdot \boldsymbol{u} = 0$, where $\nabla_s = (\boldsymbol{I} - \boldsymbol{nn}) \cdot \nabla$ is the surface-gradient operator and $\boldsymbol{n}$ is the outward-pointing unit normal vector. The spontaneous curvature c_0 takes into account any bilayer asymmetry due to differences in chemical composition or embedded proteins. For the experimental studies described in the introduction, the lipid bilayer is mostly one component, so c_0 is nearly zero. We only consider the case $c_0 = 0$ in our study, although for many vesicles *in vivo*, the spontaneous curvature may be significant (Seifert 1997). We note

that the Helfrich model does not include shear deformation or dilatation, which is present in more complicated biological membranes, such as those of cells.

The first variation of the interfacial energy (2.3) gives the force per unit area on the surrounding fluids due to the membrane's bending and surface tension. These forces, denoted as f_B and f_σ, must be balanced by the jump in viscous stresses across the interface: $[[T \cdot n]] = f_B + f_\sigma$. Expressions for f_B and f_σ are (Zhong-Can & Helfrich 1989):

$$\left.\begin{aligned} f_B &= \kappa(4KH - 4H^3 - 2\nabla_s^2 H)n \\ f_\sigma &= 2\sigma H n - \nabla_s \sigma. \end{aligned}\right\} \tag{2.4}$$

In the above equation, K is the Gaussian curvature of the interface. The convention we use is such that the mean curvature for a unit sphere is one.

To determine the motion of the vesicle's interface, we solve the Stokes velocity field (2.2) subject to continuity of velocity across the interface, surface incompressibility $\nabla_s \cdot u = 0$, and the interfacial force balance $[[T \cdot n]] = f_B + f_\sigma$. In this study, we characterize the stability of steady-state vesicles by the following procedure.

(a) We find the vesicle shape such that its normal velocity on the interface is zero: $u \cdot n = 0$. This shape is the steady-state vesicle shape.

(b) We perturb the shape infinitesimally, and solve for the velocity field on the interface. If the surface velocity causes the perturbation to amplify, the shape is unstable. By spanning a large set of possible perturbations, we can construct a set of normal modes for the deformation, as well as its associated spectrum (i.e. growth rates).

The details of these two steps depend on the numerical method we implement. In §2.3, we describe a multipole technique to solve for the velocity around an axisymmetric vesicle. We employ this technique for most of this paper, and we will verify the results with boundary integral simulations that we describe in §2.4. In the next section (§2.2), we will describe the non-dimensionalization of our equations and the important dimensionless parameters in our study.

2.2. *Non-dimensionalization and dimensionless parameters*

Because the vesicle's membrane and interior fluid are incompressible, the area (A) and the volume (V) of the vesicle are constant during deformation. We therefore non-dimensionalize all distances by the equivalent radius $a = \sqrt{A/(4\pi)}$, time scales by $\dot\epsilon^{-1}$, velocities by $\dot\epsilon a$, surface tensions by $\mu_{out}\dot\epsilon a$, and stresses by $\mu_{out}\dot\epsilon$. With this choice of non-dimensionalization, we obtain three dimensionless groups that are important in our study:

$$\nu \equiv \frac{3V}{4\pi a^3}, \quad Ca \equiv \frac{\mu_{out}\dot\epsilon a^3}{\kappa}, \quad \lambda \equiv \frac{\mu_{in}}{\mu_{out}}. \tag{2.5a–c}$$

The first parameter, the reduced volume, measures the degree of asphericity of the vesicle. It is closely related to the particle's aspect ratio, with $\nu = 1$ representing a perfect sphere, while $\nu \ll 1$ represents a high-aspect-ratio particle. The vesicles in Kantsler *et al.* (2008a) have reduced volume in the range $\nu \approx 0.25$–0.65, while those in Spjut (2010) have reduced volumes between $0.7 < \nu < 0.8$.

The second parameter is the capillary number, which is the ratio of viscous to bending stresses at the vesicle's interface. Most artificially made liposomes have a bending modulus of order 10^{-19} J (Rawicz *et al.* 2000; Pan *et al.* 2008), which leads to a capillary number of $Ca \sim O(1)$ for the experiments we consider. In this study,

we will examine the entire range of this parameter, from the no-flow limit ($Ca = 0$) to the no-bending limit ($Ca \to \infty$).

The last dimensionless group is the viscosity ratio between the inner and outer fluid. For the experiments we described, the inner fluid is the same as the outer one, so $\lambda = 1$. We will examine several viscosity ratios in the range $\lambda \sim O(1)$, and we will show that this parameter has a very weak effect on the critical condition of shape instability.

In what follows, all quantities will be written in non-dimensional form unless otherwise specified. The far-field velocity and stress boundary conditions in uniaxial extensional flow transform to

$$\boldsymbol{u}^\infty = z\hat{\boldsymbol{z}} - \tfrac{1}{2}x\hat{\boldsymbol{x}} - \tfrac{1}{2}y\hat{\boldsymbol{y}} \tag{2.6}$$

$$\left.\begin{aligned} [[\boldsymbol{T} \cdot \boldsymbol{n}]] &= \boldsymbol{f}_\sigma + Ca^{-1}\boldsymbol{f}_B \\ \boldsymbol{f}_B &= (4KH - 4H^3 - 2\nabla_s^2 H)\boldsymbol{n} \\ \boldsymbol{f}_\sigma &= 2\sigma H\boldsymbol{n} - \nabla_s\sigma. \end{aligned}\right\} \tag{2.7}$$

2.3. *Multipole method*

2.3.1. *Spheroidal coordinates and multipole expansion*

In § 3, we find that the steady-state shape of a vesicle in uniaxial flow approaches a prolate spheroid in the limit of no bending forces ($Ca \to \infty$). Motivated by this fact, we choose to parameterize the shape of the particle in spheroidal coordinates, and find a series solution (i.e. multipole expansion) to the Stokes flow equations in this geometry. We give a brief review of prolate spheroidal coordinates below, and then develop the multipole expansion shortly afterwards. We expect our multipole expansion to be accurate as long as the vesicle shape is reasonably close to spheroidal, which we will verify *a posteriori* via comparisons with boundary integral simulations (§ 2.4).

In spheroidal coordinates, a point in space is characterized by the triad (τ, ξ, ϕ). A surface of constant τ is an ellipsoid, while ϕ and $\theta = \cos^{-1}(\xi)$ are the azimuthal and polar angles (figure 3). The coordinate system additionally has a *reference ellipsoid*, described by a parameter c which is the product between its eccentricity and aspect ratio. The choice of reference ellipsoid is arbitrary, but we typically choose it to be reasonably close to the vesicle's shape. In this situation, the radial coordinate τ will be close to constant along the vesicle's interface, which will allow our multipole expansion to converge more rapidly.

Let b be the semi-minor axis length of a prolate spheroid with a reduced volume ν (this value is uniquely defined). The conversion between Cartesian and spheroidal coordinates is

$$\begin{cases} x = cb\sqrt{\tau^2 - 1}\sqrt{1 - \xi^2}\cos(\phi) \\ y = cb\sqrt{\tau^2 - 1}\sqrt{1 - \xi^2}\sin(\phi), \qquad \tau > 1, \ -1 \leqslant \xi \leqslant 1, \ 0 \leqslant \phi < 2\pi. \\ z = cb\tau\xi \end{cases} \tag{2.8}$$

The reference spheroid is a surface of constant τ with $\tau = \sqrt{1 + 1/c^2}$. The aspect ratio of this spheroid is $\sqrt{1 + c^2}$, and its focal length is cb.

In this coordinate system, the set of harmonic functions (i.e. functions G that satisfy $\nabla^2 G = 0$) is (Hobson 1931):

$$\left.\begin{aligned} \textit{Growing:} \quad & S_n^{m,(grow)} = P_n^m(\tau)P_n^m(\xi)\exp(\mathrm{i}m\phi), \\ \textit{Decaying:} \quad & S_n^{m,(decay)} = Q_n^m(\tau)P_n^m(\xi)\exp(\mathrm{i}m\phi). \end{aligned}\right\} \tag{2.9}$$

In the above equation, $P_n^m(x)$ and $Q_n^m(x)$ are Legendre functions of the first and second kind (details of which are given in § A.1). The decaying harmonics vanish at infinity, but become singular along the focal axis of the reference ellipsoid (when $\tau = 1$). Conversely, the growing harmonics are finite along the focal axis, but are singular at infinity. For an axisymmetric geometry, as we consider here for uniaxial extensional flow, the harmonic functions will have no dependence on the azimuthal angle ϕ, so we can set $m = 0$ in the equations above.

Given a set of harmonic functions, we can derive a series solution (i.e. multipole expansion) for the Stokes equations in a straightforward fashion (Tran-Cong & Blake 1982; Leal 2007). We omit the details here, and state the final results (see § A.2 for derivation). The disturbance velocity and pressure fields in axisymmetric flow are

$$u_\tau = b \frac{\sqrt{\tau^2 - 1}}{\sqrt{\tau^2 - \xi^2}} \sum_{n=0}^{\infty} \left[\frac{1}{2} \xi c_n P_n(\xi) \left(R_n(\tau) - \tau R_n'(\tau) \right) - \frac{1}{2} d_n P_n(\xi) R_n'(\tau) \right] \quad (2.10)$$

$$u_\xi = b \frac{\sqrt{1 - \xi^2}}{\sqrt{\tau^2 - \xi^2}} \sum_{n=0}^{\infty} \left[\frac{1}{2} \tau c_n R_n(\tau) \left(\xi P_n'(\xi) - P_n(\xi) \right) + \frac{1}{2} d_n R_n(\tau) P_n'(\xi) \right] \quad (2.11)$$

$$p = -\frac{\tilde{\eta}}{c(\tau^2 - \xi^2)} \sum_{n=0}^{\infty} c_n \left[\xi(\tau^2 - 1) R_n'(\tau) P_n(\xi) + \tau(1 - \xi^2) R_n(\tau) P_n'(\xi) \right]. \quad (2.12)$$

In the above equations, $R_n(\tau)$ is the radial component of the spheroidal harmonics, which is equal to $Q_n(\tau)$ outside the vesicle and $P_n(\tau)$ inside the vesicle. A prime on these functions indicates differentiation. The non-dimensional viscosity is $\tilde{\eta}$, which is one outside the particle and λ inside the particle. The coefficients $\{c_n, d_n\}$ are the multipole moments, which we have to determine. Outside the vesicle, we solve for $\{c_0, c_1, \ldots\}$ and $\{d_0, d_1, \ldots\}$. In order to avoid degeneracy in the above sums (Dassios, Payatakes & Vafeas 2004), we set $c_0 = c_1 = d_0 = 0$ and solve for $\{c_2, c_3, \ldots\}$ and $\{d_1, d_2, \ldots\}$ inside the vesicle. The series expressions for the viscous stresses are listed in § A.2.

In the next section, we discuss how we parameterize the vesicle interface, and how we determine the deformation rate of the interface.

2.3.2. *Surface parametrization and evolution equation for vesicle's shape*

In uniaxial extensional flow, the vesicle shape and tensions are independent of the azimuthal angle ϕ around the extension axis (the z axis). We can thus parameterize the shape by the level surface $\tau = g(\xi, t)$ and the tension by the function $\sigma = \sigma(\xi, t)$, where t is time. We decompose both of these quantities into Legendre modes

$$\tau = \sum_{m=0}^{\infty} g_m(t) P_m(\xi), \quad \sigma = \sum_{m=0}^{\infty} \sigma_m(t) P_m(\xi) \quad (2.13a,b)$$

and attempt to solve for the deformation rate $\partial g_m / \partial t$ as a function of the current vesicle configuration $g_m(t)$.

To do so, we first decompose the velocity field into a far-field component (2.6) and a disturbance field which is described by the multipole velocity solution (2.10) and (2.11). We perform the same decomposition for the viscous stresses (see § A.2). We then project the following interfacial boundary conditions onto a set of Legendre modes: continuity of velocity, surface incompressibility ($\nabla_s \cdot \boldsymbol{u} = 0$), the kinematic

boundary condition ($\partial g/\partial t = \boldsymbol{u} \cdot \boldsymbol{\nabla}(\tau - g)$), and the interfacial force balance ($[[\boldsymbol{T} \cdot \boldsymbol{n}]] = \boldsymbol{f}_\sigma + Ca^{-1}\boldsymbol{f}_b$). These expressions, along with conservation of area and volume

$$\frac{\mathrm{D}A}{\mathrm{D}t} = \int_S 2H(\boldsymbol{u} \cdot \boldsymbol{n})\mathrm{d}A = 0, \quad \frac{\mathrm{D}V}{\mathrm{D}t} = \int_S (\boldsymbol{u} \cdot \boldsymbol{n})\mathrm{d}A = 0 \quad (2.14a,b)$$

yield a set of linear equations for the multipole moments $\{c_n, d_n\}$ inside and outside the vesicle, the surface tension coefficients $\{\sigma_m\}$, the constant interior pressure p_0, and the deformation rate of the vesicle's interface $\{\partial g_m/\partial t\}$. We can thus solve for the deformation rate $\partial g_m/\partial t$ for a given vesicle configuration g_m, which allows us to determine the evolution of the vesicle's shape to steady state. We solve for these quantities with a cutoff mode N for the velocity and surface tension coefficients, and a cutoff mode M for the vesicle shape coefficients g_m. We typically choose N larger than M (either $N = M + 10$ or $M + 20$), as we need to resolve the velocity and tension fields more accurately in order to determine the shape at an acceptable level of accuracy. Although omitted here, § A.3 details how we calculate the bending forces in all of the calculations above. In the next section, we will describe how to find the steady-state shape of vesicles, and then follow with a determination of the stability of these shapes.

2.3.3. *Determine steady-state shapes*

To determine the steady-state shape of the vesicle, we could in principle integrate the deformation rate $\partial g_m/\partial t$ from an initial configuration $g_m(t = 0)$ to a state where the shape is nearly steady. This technique is time consuming, so we instead perform a constrained, adaptive Newton's iteration, which is a method of root-finding (see Boyd & Vandenberghe 2004, p. 531). We set the deformation rate $\{\partial g_m/\partial t\}$ to be zero, and solve for the velocity coefficients $\{c_n, d_n\}$ and surface tension coefficients $\{\sigma_1, \sigma_2, \ldots\}$ from the velocity boundary conditions and the tangential stress balance. The remaining boundary condition, the normal stress balance, yields a nonlinear equation for the vesicle shape g_m, the isotropic tension σ_0, and the isotropic pressure p_0. We solve this equation subject to the constraints of constant area and volume. At each step in Newton's iteration, we calculate the Hessian matrices using a central difference approximation. We terminate root-finding when the two-norm of the equations and constraints are between 10^{-4} and 10^{-7}, and the step size is less than 10^{-9}. To save computational time, we only solve for the even coefficients of g_m due to the symmetry of the flow.

This root-finding technique is accurate for solving nonlinear equations when the initial guess is close to the actual solution. To find the steady-state shape of a vesicle with reduced volume ν and capillary number Ca, we first start with the shape of a vesicle in the no-flow limit ($Ca = 0$), which is well known and easily calculable (see Seifert, Berndl & Lipowsky 1991). At low reduced volumes, there are multiple no-flow solutions, so we pick the branch that corresponds to a prolate shape, as this branch will be stable during uniaxial extension. Using the prolate shape as an initial guess, we use root-finding to determine the shape at a slightly higher capillary number. We keep repeating this process, i.e. using the latest solution to find the shape at an even higher Ca, until we march to the desired Ca. We find the shapes calculated from this method give good agreement with the boundary integral simulations (figure 4).

2.3.4. *Calculate growth rates*

To determine the stability of a steady-state vesicle, we add an infinitesimal perturbation $\delta g(\xi, t)$ to the level shape $\tau = g(\xi, t)$, and decompose this perturbation

(a)

$v = 0.80$

$Ca = 1$

$Ca = 10$

$Ca = 100$

$v = 0.65$

$Ca = 1$

$Ca = 10$

$Ca = 100$

(b)

$v = 0.57$

$Ca = 0$

$Ca = 1.4$

$Ca = 1.6$

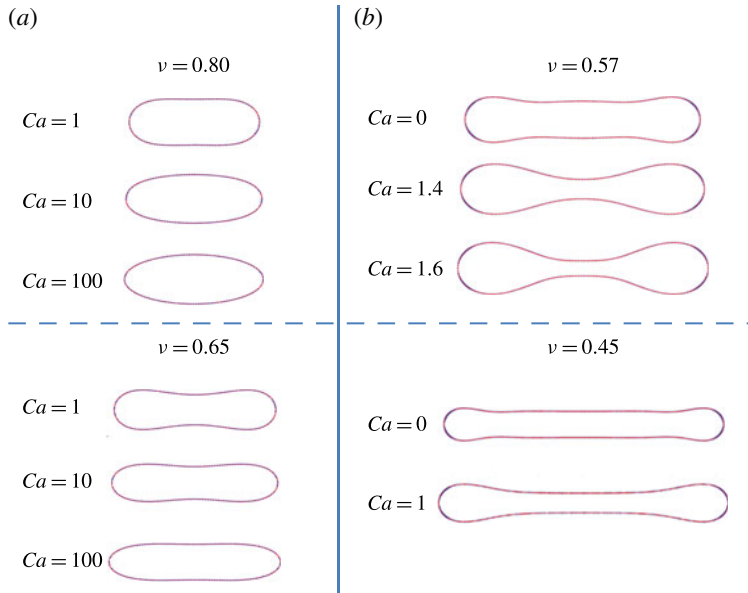$v = 0.45$

$Ca = 0$

$Ca = 1$

FIGURE 4. (Colour online) Steady-state shapes in uniaxial extensional flow. (a) Intermediate-aspect-ratio particles. (b) High-aspect-ratio particles. The crosses (blue online) are boundary integral simulations, while the curves (red online) are results from a multipole expansion. Both results are indistinguishable from each other. For (a), the boundary integral simulations are from Zhao & Shaqfeh (2013b), while for (b), the boundary integral simulations are from this study (see § 2.4 for description). The viscosity ratio is $\lambda = 1$ for all shapes. The number of modes we use for the multipole expansion is $M = 15$ even modes for (a) and $M = 20$ even modes for (b). When compared with the no-flow solution ($Ca = 0$), we use a very small capillary number ($Ca = 10^{-3}$) in the multipole expansion.

into a set of modes

$$\delta g(\xi, t) = \sum_{m=0}^{M} a_m(t) w_m(\xi), \qquad (2.15)$$

where each mode w_m conserves area and volume up to $O(\delta^2)$, i.e.

$$\int_{-1}^{1} (g^2 - \xi^2) w_m(\xi) \, d\xi = 0, \qquad \int_{-1}^{1} H(g^2 - \xi^2) w_m(\xi) \, d\xi = 0. \qquad (2.16a,b)$$

(Note that these equations are a restatement of (2.14) when integrated around the base-state shape.) For each individual coefficient a_m, we solve the vesicle's deformation rate $\partial g / \partial t$, and project this quantity onto the modes w_m, which yields one column of the dispersion matrix for a linear stability analysis. The eigenvalues of this matrix give the growth rates of shape perturbations, while the eigenfunctions give the deformation modes of the vesicle (which are linear combinations of the modes w_m). The magnitude of the deformation we apply in our analysis is $a_m \sim O(10^{-5})$. When solving for the deformation rates, we linearize all boundary conditions exactly except the mean curvatures and bending forces, which we approximate using central differences with perturbation magnitude a_m. The growth rates we calculate from this procedure match well with results from boundary integral simulations (figure 5).
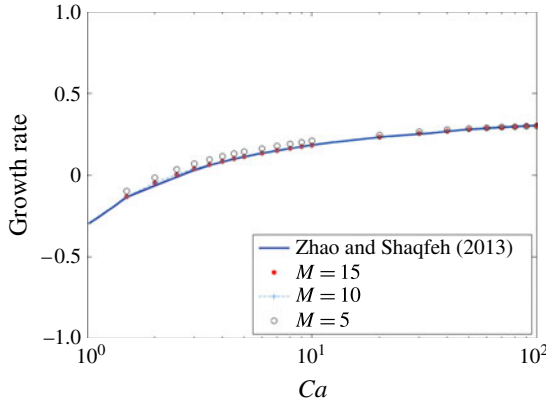
FIGURE 5. (Colour online) Growth rate calculations: multipole versus boundary integral. The above plot is the growth rate of the most unstable, non-translating mode versus *Ca*. The reduced volume is $\nu = 0.65$ and the viscosity ratio is $\lambda = 1$. The solid line (blue online) shows boundary integral results from Zhao & Shaqfeh (2013*b*), while the symbols are results from our multipole expansion (§ 2.3). Here *M* is number of even modes we use in our expansion. For a discussion, see § 3.4.

2.4. *Boundary integral technique*

We utilize the boundary integral techniques described in Spann, Zhao & Shaqfeh (2014) to quantify the dynamics of vesicles in extensional flows, and to compare with our multipole expansion. We give a brief overview here, and allow the reader to view the remaining details in that publication.

Under the assumption of Stokes flow, the velocity field on the surface of the vesicle satisfies the integral equation (Pozrikidis 1992):

$$\frac{1+\lambda}{2}u_j(\boldsymbol{x_0}) \;=\; u_j^\infty(\boldsymbol{x_0}) + \frac{1}{8\pi}\int_S G_{ij}(\boldsymbol{x},\boldsymbol{x_0})[[f_i]](\boldsymbol{x})\,\mathrm{d}S(\boldsymbol{x})$$
$$+ \frac{1-\lambda}{8\pi}\int_S T_{ijk}(\boldsymbol{x},\boldsymbol{x_0})u_i(\boldsymbol{x})n_k(\boldsymbol{x})\,\mathrm{d}S(\boldsymbol{x}). \tag{2.17}$$

In the above equation, we assume Einstein notation (where repeated indices are summed). The quantity $[[f_i]]$ is the jump in hydrodynamic stresses across the interface, which for our problem is the sum of surface tension and bending contributions: $[[\boldsymbol{f}]] = \boldsymbol{f}_\sigma + Ca^{-1}\boldsymbol{f}_B$. The functions G_{ij} and T_{ijk} are the standard point force and point dipole (stresslet) solutions to Stokes flow in infinite space:

$$G_{ij}(\boldsymbol{x},\boldsymbol{x_0}) = \frac{\delta_{ij}}{r} + \frac{\tilde{x}_i\tilde{x}_j}{r^3}, \quad T_{ijk}(\boldsymbol{x},\boldsymbol{x_0}) = -6\frac{\tilde{x}_i\tilde{x}_j\tilde{x}_k}{r^5} \tag{2.18a,b}$$

where $\tilde{x} = x - x_0$ and $r = |\tilde{x}|$. The boundary integral equations (2.17), along with the surface incompressibility constraint $\nabla_s \cdot \boldsymbol{u} = 0$, is sufficient to determine the velocity and surface tension fields along the interface.

We discretize the vesicle into piecewise triangular elements, with the number of faces ranging from 5000 to 20 000 elements depending on the aspect ratio of the particle. We calculate the bending forces on each element using the virtual work

principle. We note that care must be taken when evaluating the bending forces on the surface of the particle, as an accurate estimate for the derivative of the curvature is necessary. For vesicles, we calculate the bending energy on a smooth C^1 surface constructed by Loop subdivision (Spann *et al.* 2014). After determining the velocity fields on the interface, we update the position of each vertex using a standard Forward Euler scheme: $\boldsymbol{x}_{n+1} = \boldsymbol{x}_n + \Delta t u_n(\boldsymbol{x}_n) + \beta \Delta t u_t(\boldsymbol{x}_n)$, where u_n is the normal velocity, u_t is the tangential velocity, and β is a factor chosen such that the points do not cluster. A routine for a good choice of the relaxation parameter β is given by Spann *et al.* (2014).

To determine the stability of a vesicle at a given capillary number, viscosity ratio and reduced volume, we first form a cylindrical vesicle, and relax the particle in zero flow ($Ca = 0$) until it reaches a prolate equilibrium shape (this shape is locally stable, but not globally stable at low reduced volumes (see Seifert *et al.* 1991)). We then turn on the flow, and allow the vesicle to relax to steady state (in our case, when the velocity field is $O(10^{-3})$ or less). To determine the stability of this shape, we add a small sinusoidal perturbation

$$r(z) = r_0(z) + \epsilon \sin(2\pi z/z_{max}) \tag{2.19}$$

where r is the distance from the interface to the axis of extension, and ϵ is a small number, usually of order 0.01 times the original radius r_0. We track the normal component of the surface velocity over time, and if this magnitude grows, the shape is unstable. To measure the growth rates more accurately for the case of uniaxial extensional flow, we normalize the vesicle length by z_{max} and then fit the radius r to a set of Legendre polynomials (we use 32 modes). The largest growth rate of the Legendre modes corresponds to the growth rate of the instability. See Spann *et al.* (2014) for more details.

The boundary integral technique can handle more general geometries and flow types than the multipole method discussed in §2.3. However, the multipole method is much less computationally intensive. For example, the multipole method determines the steady-state shape and growth rates of a vesicle (at fixed ν, λ and Ca) in a few minutes on a single processor, while the full 3D boundary integral simulations takes approximately 1 day on a computer cluster (≈ 60 processors). Our boundary integral simulations show that the two most unstable modes in uniaxial flow are indeed axisymmetric, so we have confidence in using the multipole method to understand the stability of a vesicle.

3. Results: intermediate-aspect-ratio vesicles

In this section, we describe the shape transitions of intermediate-aspect-ratio vesicles in extensional flows, which correspond to the experimental observations in Spjut (2010). We first examine the limiting case of no bending at the vesicle's interface (i.e. $Ca \to \infty$), and determine the physical processes that destabilize the vesicle shape. We find that the mechanism for instability is similar to the Rayleigh–Plateau phenomenon (i.e. capillary breakup of a viscous thread). When a vesicle is subject to an asymmetric shape perturbation, the interface's curvature change will induce a pressure-driven flow in the interior of the particle. This flow amplifies the perturbation when the vesicle is above a critical aspect ratio, which in turn creates an asymmetric dumbbell. In §4, we find that this mechanism is the appropriate one even at finite capillary number. We quantify the critical extension rates for this shape transition and discuss how the stability criterion depends on the reduced volume and viscosity ratio.
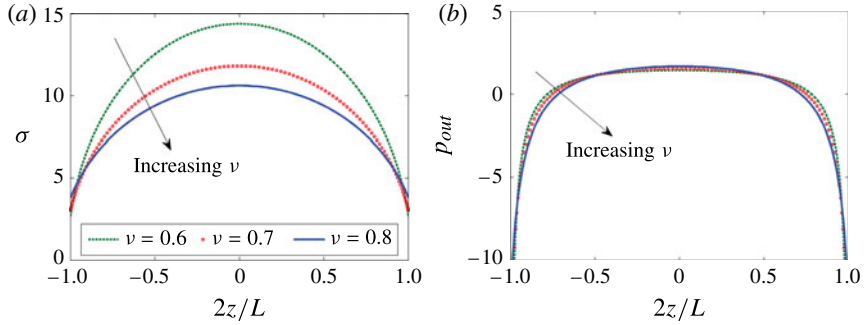
FIGURE 6. (Colour online) Base-state tensions and pressures: intermediate-aspect-ratio particles at infinite *Ca*. (*a*) Base-state tensions. (*b*) Base-state outer pressure along the interface. The quantity L is the length of the vesicle, with $z = \pm L/2$ corresponding to the ends of the vesicle.

3.1. *No bending limit: shapes, tensions and growth rates*

In two of our previous publications (Spann *et al.* 2014; Zhao & Shaqfeh 2013*b*), we performed boundary integral simulations of vesicles in uniaxial extensional flows, and determined their steady state shapes for a variety of extensional rates (i.e. *Ca*) and aspect ratios (i.e. reduced volume ν). A plot of these shapes is shown in figure 4(*a*). As the capillary number increases, we observe that the shapes become more ellipsoidal. Because these shapes approach a convenient geometry, we can develop an analytical theory to determine the vesicle shapes in the limit of very high *Ca* (well beyond the range in these published papers). We parameterize the shape using spheroidal coordinates, and then solve for Stokes flow around the shape, using the multipole expansion discussed in § 2.3. In doing so, we find that the vesicle takes the shape of an *exact spheroid when its interface has no bending resistance* ($Ca = \infty$). A vesicle can achieve such a steady shape due to the incompressibility of its membrane, which strongly resists deformation at high extension rates. This result is not true for the standard droplet case, where no steady state exists at very large extension rates, and hence the droplet breaks.

The derivation of the vesicle shape and its associated tensions, in the limit of no bending ($Ca \to \infty$), is found in § A.4. We plot the base-state tensions and pressures in figure 6. The surface tensions are parabolic, with the maximum at the middle of the particle. As the aspect ratio increases (or the reduced volume decreases), the surface tension gradients become larger. We observe a similar trend for the outer pressure on the interface, except that the profiles are more 'blunt' than the surface tension profiles. These trends for pressure and tensions make sense physically. The extensional flow stretches the vesicle by creating a higher-pressure region at the centre of the particle and a low-pressure region at the ends. Because the membrane is area preserving, this stretching induces a parabolic tension that attempts to restore the vesicle to its original (equilibrium) shape. At steady state, these processes balance each other and the net velocity of the interface is zero. As far as we know, we are unaware of any studies that have examined the shape, tensions, and pressures of a vesicle in the limit of no bending. Although most experimental studies examine vesicles with finite *Ca*, the results in the $Ca \to \infty$ limit provide physical insight into the dynamics and stability of vesicles with finite bending. Furthermore, an interface with no bending in the Helfrich model (2.3) corresponds to a particle with only an area-preserving membrane, which
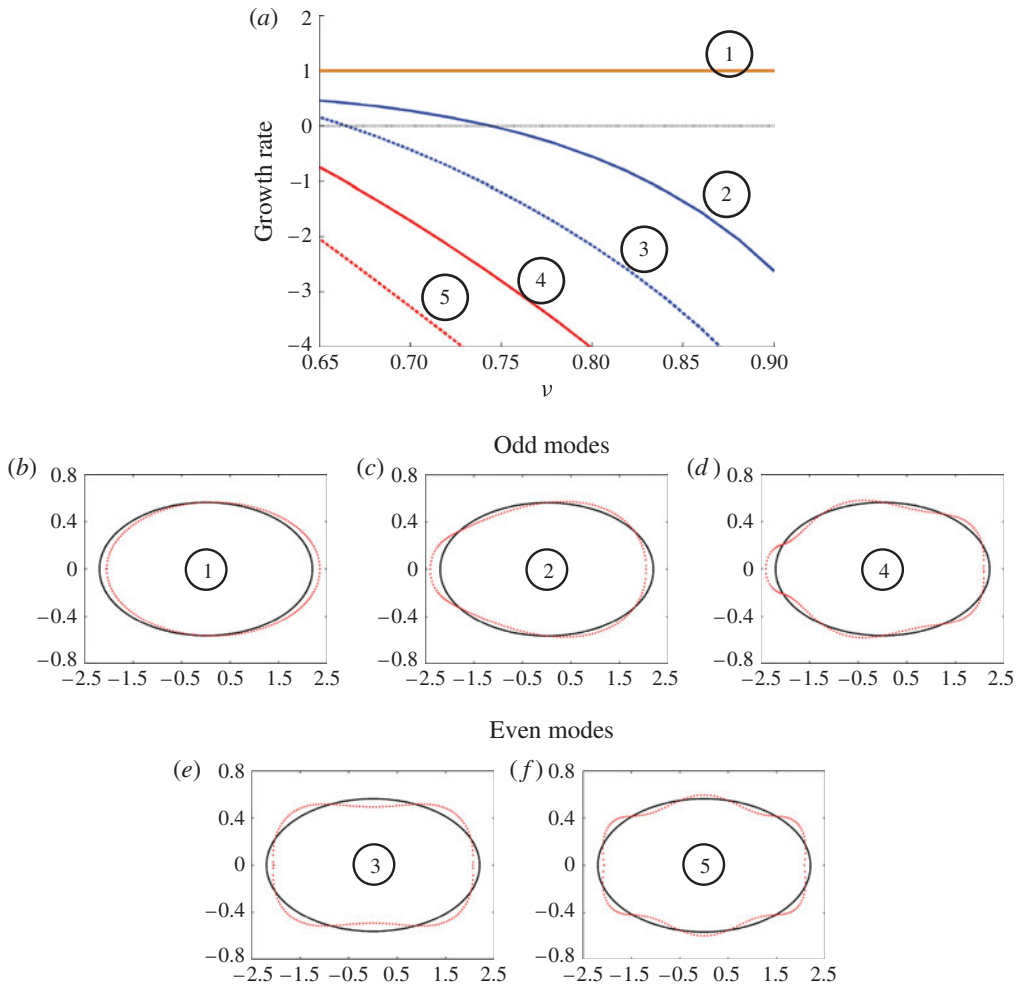
FIGURE 7. (Colour online) Growth rates for intermediate-aspect-ratio vesicles, no bending ($Ca = \infty$). The top graph plots the growth rates versus reduced volume for the first five deformation modes of the vesicle. The modes at $\nu = 0.7$ are at the bottom. Mode 2 corresponds to the pear-shaped instability observed by Spjut (2010). The shapes are not to scale. All results are at viscosity ratio $\lambda = 1$.

is a model for many other types of complex interfaces, such as droplets with strongly adsorbed surfactants (see Blawzdziewicz, Cristini & Loewenberg 1999; Timmermans & Lister 2002). For such surfactant-laden interfaces, the limit of large surface tension gradients, or large Marangoni number, gives the same interfacial force balance as the Helfrich model with $Ca \to \infty$.

We characterize the stability of the base-state vesicle shape by perturbing its interface infinitesimally, solving the velocity field around the particle, and finding the conditions under which the velocity amplifies the perturbation (see § 2.3). We can further decompose the deformation into normal modes and find their corresponding growth rates. Figure 7 shows the growth rates and shapes of the five most unstable modes at matched viscosity ratio ($\lambda = 1$) and no bending ($Ca \to \infty$). The most
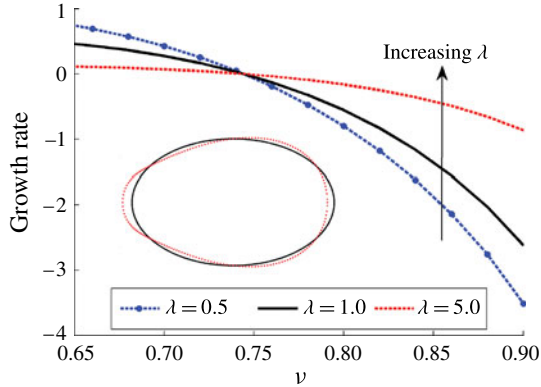
FIGURE 8. (Colour online) Variation of growth rate with viscosity ratio. This plot examines the growth rate of the pear-shaped mode (inset) in the limit of no bending ($Ca \to \infty$). We show in § 3.2 that the onset of instability is independent of the viscosity ratio, as this graph demonstrates.

unstable mode, with growth rate unity, is translation, which is of no concern to us. This result means that a vesicle will move away from the extensional flow if its centre of mass no longer coincides with the stagnation point. The second most unstable mode is an asymmetric 'pear' shape, which looks remarkably similar to the shapes observed by Spjut (2010) at the onset of instability. In fact, if we evolve this perturbed shape over time, we observe transitions of the form in figure 2(*a*,*b*). This mode is stable (i.e. growth rates are negative) when the vesicle is at low aspect ratio, but unstable when the aspect ratio exceeds a critical value ($\nu < 0.75$). These results are consistent with previous simulations by Zhao & Shaqfeh (2013*b*).

The other modes of the spectrum have lower growth rates, and hence are unlikely to be observed in experiments (e.g. in the case of Spjut). Nevertheless, the next mode looks like capillary pinch-off (i.e. formation of a central neck with bulbous ends). For the rest of this section (§ 3), we will focus our discussion on the experimentally relevant second mode, which is the asymmetric pear shape.

Figure 8 shows how the growth rate of the pear shape mode varies with viscosity ratio, in the limit of no bending ($Ca \to \infty$). As the viscosity ratio increases, the vesicle behaves more like a solid particle, which lowers the growth rate when the vesicle is unstable. We observe the opposite trend when the viscosity ratio decreases (or when the vesicle becomes more like a bubble). One interesting fact to note is that the viscosity ratio does not appear to change the onset of the instability, which is when the growth rate becomes zero. It turns out that this observation is true for all values of Ca, as long as the flow around the particle is uniaxial. We prove this statement in the next subsection, as well as develop a framework to determine the mechanism of the instability.

3.2. *Evolution equation for perturbation energy*

In this section, we will prove that the onset of a shape instability is independent of the viscosity ratio (λ), as long as flow around the particle is axisymmetric. To begin, let us take the interfacial force balance, multiply by the velocity and integrate over the surface of the vesicle. This process gives the production and dissipation of energy
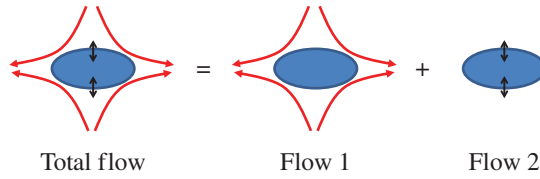
FIGURE 9. (Colour online) Decomposition of flow in § 3.2.

on the membrane's surface:

$$\int_S \boldsymbol{u} \cdot [[\boldsymbol{T} \cdot \boldsymbol{n}]] \, \mathrm{d}A = \int_S \boldsymbol{u} \cdot \left(\boldsymbol{f}_\sigma + Ca^{-1} \boldsymbol{f}_B \right) \, \mathrm{d}A. \tag{3.1}$$

In the above equation, the left-hand side is the rate of energy dissipation due to viscous forces, while the right-hand side is the rate of energy production due to bending and surface tension. We will linearize all fields around a steady-state configuration and determine an evolution equation for the perturbation energy, which in turn will provide insight into the processes that destabilize the interface.

Before we begin, we will rewrite the energy balance (3.1) in a more convenient form. Recall the velocity and tangential stress boundary conditions for a vesicle under extensional flow:

$$\left.\begin{array}{llll} \text{Far field:} & \boldsymbol{u} \to \boldsymbol{E} \cdot \boldsymbol{x} & \text{as } \boldsymbol{x} \to \infty \\ \text{Continuity of velocity:} & [[\boldsymbol{u}]] = 0 & \text{on interface} \\ \text{Surface incompressibility:} & \boldsymbol{\nabla}_s \cdot \boldsymbol{u} = 0 & \text{on interface} \\ \text{Kinematic:} & \boldsymbol{u} \cdot \boldsymbol{n} = \dfrac{1}{\|\boldsymbol{\nabla}(\tau - g)\|} \dfrac{\partial g}{\partial t} & \text{on interface} \\ \text{Tangential stress:} & [[\boldsymbol{t} \cdot \boldsymbol{T} \cdot \boldsymbol{n}]] + \boldsymbol{t} \cdot \boldsymbol{\nabla}_s \sigma = 0 & \text{on interface.} \end{array}\right\} \tag{3.2}$$

In the above expressions, $\boldsymbol{E} = (\boldsymbol{\nabla}\boldsymbol{u}^\infty + \boldsymbol{\nabla}\boldsymbol{u}^{\infty,T})/2$ is the far-field rate of extension, while $\partial g/\partial t$ is the deformation rate of the membrane when it is parameterized as $\tau = g(\xi)$ in spheroidal coordinates. Let us now define the velocity, tension and stress fields as follows:

$$\boldsymbol{u} = \boldsymbol{u}^{(1)} + \boldsymbol{u}^{(2)}, \quad \boldsymbol{T} = \boldsymbol{T}^{(1)} + \boldsymbol{T}^{(2)}, \quad \sigma = \sigma^{(1)} + \sigma^{(2)}, \tag{3.3a–c}$$

where all terms with a superscript (1) satisfy boundary conditions (3.2) with $\partial g/\partial t = 0$, while all terms with a superscript (2) satisfy boundary conditions (3.2) with $\boldsymbol{E} = 0$. Physically, flow (1) represents the extensional flow around a non-deforming, incompressible interface, while flow (2) represents the flow due to a deforming, incompressible interface that is in a fluid otherwise at rest (see figure 9). These two flow fields are not independent of each other, as they are linked through the normal stress boundary condition: $[[p]] + 2\sigma H + Ca^{-1}f_B = 0$. One interesting fact we can show is that flow (1) is equivalent to flow around a rigid particle, as long as the extensional flow is axisymmetric. To demonstrate this fact, we note that flow (1) must vanish on the vesicle's surface since its normal component is zero and it has zero surface divergence and zero surface curl.

We now substitute the expressions of (3.3) into the energy balance (3.1). Noting that the tangential boundary condition is automatically satisfied for flow (1), the energy expression becomes

$$\int_S \boldsymbol{u}^{(2)} \cdot [[\boldsymbol{T}^{(2)} \cdot \boldsymbol{n}]] \, \mathrm{d}A - \int_S \boldsymbol{u}^{(2)} \cdot \boldsymbol{f}_\sigma^{(2)} \, \mathrm{d}A = \int_S u_n^{(2)} \left(Ca^{-1}f_B + [[p]]^{(1)} + 2\sigma^{(1)}H \right) \mathrm{d}A. \tag{3.4}$$

The interpretation of the above expression is as follows. The first term on the left-hand side is the dissipation due to a purely deforming interface, which is a strictly negative quantity. The second term is the work done by surface tension when the interface deforms in the absence of flow. From the virtual work principle, we can show that this term is strictly zero, as it is the work provided by a constraint force. On the right-hand side, the first term is the dissipation from bending forces. The last two terms are energy coupling terms created by the interaction of flow (2) and flow (1). The coupling is between the interfacial velocity $u_n^{(2)}$ and the sum of pressure and capillary forces from flow (1) (which is flow around a rigid body).

Let us now consider a vesicle at steady state, where the deformation rate of the membrane is initially zero. We perturb the shape infinitesimally, and expand the energy balance (3.4) to quadratic order in the perturbations. Let us define the perturbed shape as $\tau = g_{base}(\xi) + \delta g(\xi) \exp(st)$, where s is the growth rate of the shape perturbation ($s > 0$ indicates instability). We expand all terms related to flow field (1) as

$$\boldsymbol{u}^{(1)} = \boldsymbol{u}_{base}^{(1)} + \delta \boldsymbol{u}^{(1)} \exp(st), \quad \sigma^{(1)} = \sigma_{base}^{(1)} + \delta \sigma^{(1)} \exp(st), \quad \boldsymbol{T}^{(1)} = \boldsymbol{T}_{base}^{(1)} + \delta \boldsymbol{T}^{(1)} \exp(st).$$
$$(3.5a\text{–}c)$$

We similarly expand all terms related to flow field (2) as

$$\boldsymbol{u}^{(2)} = s\delta \tilde{\boldsymbol{u}}^{(2)} \exp(st) = s\delta \boldsymbol{x} \exp(st), \quad \sigma^{(2)} = s\delta \tilde{\sigma}^{(2)} \exp(st), \quad \boldsymbol{T}^{(2)} = s\delta \tilde{\boldsymbol{T}}^{(2)} \exp(st),$$
$$(3.6a\text{–}c)$$

where $\delta \boldsymbol{x}$ is the deformation of the interface. All quantities related to flow (2) are linear in the deformation rate $\partial g/\partial t$, so they are linear in the growth rate s, as indicated by the above equation. When we substitute the expansions (3.5) and (3.6) into the energy balance (3.4), we obtain a final expression for the evolution equation of the perturbation energy:

$$-s \int_S \delta \boldsymbol{x} \cdot \delta [[\tilde{\boldsymbol{T}}^{(2)} \cdot \boldsymbol{n}]] \, \mathrm{d}A = \int_S \delta x_n (-[[\delta p]]^{(1)} - 2\delta \sigma^{(1)} H - 2\sigma^{(1)} \delta H - Ca^{-1} \delta f_B) \, \mathrm{d}A. \quad (3.7)$$

This equation determines the perturbation growth rates of the instability. The integral multiplying $-s$ is the viscous dissipation due to the deforming membrane, which is a negative quantity. The first two terms on the right-hand side are the energy production from the perturbation pressure and surface tension of rigid body flow (flow 1). The last two terms are the energy production from the perturbation curvature and bending forces. The shape perturbation is unstable when the growth rate s is positive and, hence, when the entire right-hand side is positive. *Thus, by examining the energy contributions from pressure, surface tension, curvature, and bending, we can determine the mechanism by which a steady-state vesicle becomes unstable*. These energy contributions also determine the stability threshold, which is the condition under which the growth rate s is zero. Since the right-hand side of (3.7) is independent of the viscosity ratio λ, the stability threshold is independent of this parameter as well. However, the *magnitude* of the growth rates depends on λ, as the viscous dissipation on the left-hand side varies considerably with this parameter.

When we derived (3.7), we made two major assumptions: axisymmetric flow and an incompressible membrane. If we relax the first assumption (by using planar extensional flow), the equation does not change. However, the base-state flow $\boldsymbol{u}^{(1)}$ will no longer be equivalent to flow around a rigid particle and, hence, the stability threshold will depend on the viscosity ratio, albeit weakly. If we relax the second assumption, the equation will have additional terms on the right-hand side that involve the dilatation of the membrane. We do not explore these effects in this paper.
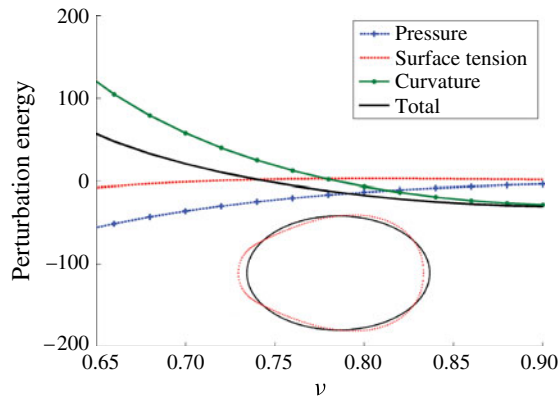
FIGURE 10. (Colour online) Perturbation energy for intermediate-aspect-ratio vesicles, in the limit of no bending ($Ca \rightarrow \infty$). We plot the perturbation energies versus reduced volume for the pear-shaped mode (inset) in the limit of no-bending forces ($Ca \rightarrow \infty$). The definitions of the pressure, surface tension and curvature contributions are in (3.7). The convention we employ is that positive energies are destabilizing. As the aspect ratio increases (i.e. reduced volume decreases), the curvature energy destabilizes the membrane. The reference spheroid we choose in our calculations coincides with the vesicle shape.

In the next section, we will examine the energy contributions from pressure, surface tension, curvature, and bending for the pear shape mode, which is the mode that corresponds to the shape transitions observed by Spjut (2010). We will find that the curvature energy is most responsible for the destabilization of the steady-state shape, and this effect can be explained by a modified Rayleigh–Plateau instability.

3.3. *Mechanism for instability: no-bending limit*

In this section, we plot the perturbation energies as described by (3.7) for the pear-shaped mode, which is the mode that corresponds to the shape transitions observed in experiments by Spjut (2010) and in simulations by Zhao & Shaqfeh (2013b). By examining how the energy contributions vary with the particle aspect ratio (or reduced volume), we can determine the physical processes that destabilize the steady-state vesicle.

Figure 10 shows the perturbation energies for the pear-shaped mode in the limit of no bending ($Ca \rightarrow \infty$). The convention in these plots is that positive energy destabilizes the shape, while negative energy stabilizes. We see that the pressure contribution is negative (i.e. stabilizing), while the surface tension contribution is negligible. What is interesting is that the curvature contribution changes greatly with the aspect ratio of the particle, being negative (i.e. stabilizing) for nearly spherical particles, but positive (i.e. destabilizing) for elongated particles. This analysis suggests that curvature changes on the interface dominate the dynamics and stability of the vesicle. Below, we offer a physical explanation.

When a steady-state vesicle changes its geometry, the shape change induces a force on the interface proportional to the curvature-induced pressure $\delta p_{curv} = 2\delta H \sigma$, where σ is the base-state tension, and δH is the change in the interface's curvature. If this pressure is low in the regions of swelling, and high in the regions of contraction, the induced flow will amplify the shape perturbation, and hence create an instability. This
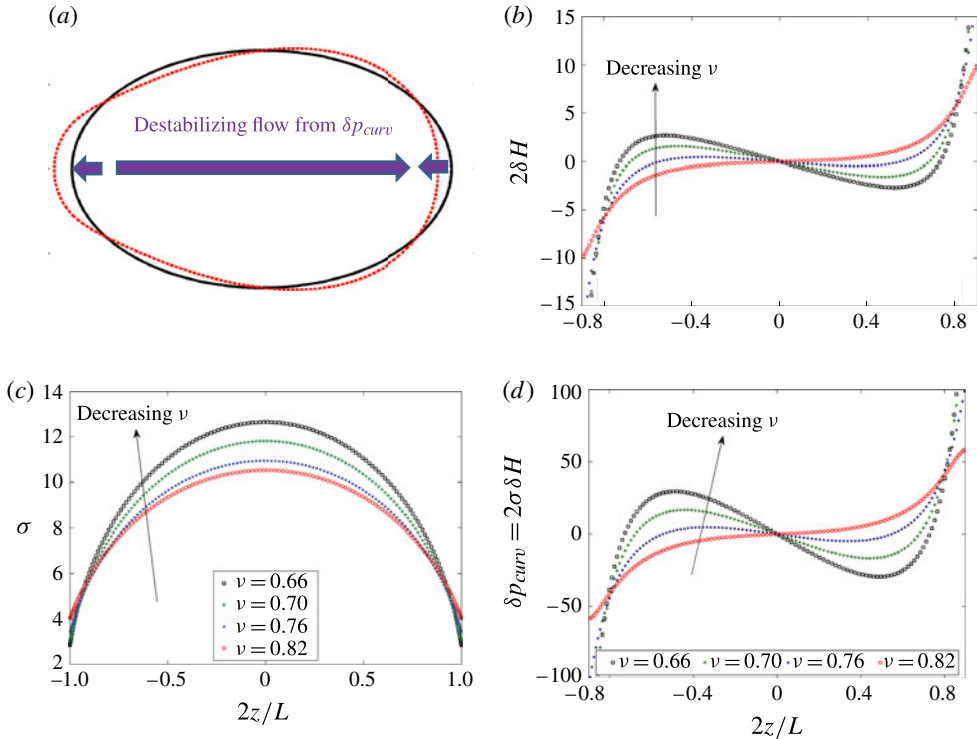
FIGURE 11. (Colour online) Curvature pressure, no bending limit. (*a*) Schematic of base-state shape (solid black line) and pear-shaped mode (dotted line, red online). (*b*) Curvature change $2\delta H$ induced by the pear-shaped mode. (*c*) Base-state surface tension σ. (*d*) Curvature pressure $\delta p_{curv} = 2\sigma\delta H$. For low reduced volumes (i.e. high aspect ratios), the curvature pressure induces a flow indicated by the purple arrows in (*a*). This flow amplifies the perturbation and, hence, destabilizes the membrane.

argument is similar to that made for the Rayleigh–Plateau phenomenon (Tomotika 1935), which describes the stability of a cylindrical column of liquid to sinusoidal perturbations. To see if our intuition is reasonable, we plot the curvature-induced pressure of the pear-shaped mode, for a wide variety of aspect ratios (i.e. reduced volumes). Figure 11(*a*) shows a schematic of an ellipsoidal vesicle perturbed by the pear-shaped mode. Figure 11(*b*) presents δH associated with this mode, and figure 11(*c*) shows the base-state tensions (σ). We see that for high-aspect-ratio particles (i.e. low reduced volume), the curvature decreases in the regions of swelling, and increases in the regions of contraction (figure 11*b*). The parabolic tensions amplify this effect, and thus the curvature-induced pressure (figure 11*d*) creates a flow that destabilizes the shape perturbation (as indicated by arrows in figure 11*a*). When the aspect ratio is small (i.e. reduced volume is close to one), the curvature change shows the opposite trend: it increases in the regions of swelling and decreases elsewhere. In this situation, the curvature-induced pressure stabilizes shape perturbations.

In the next section, we will demonstrate that the instability mechanism is similar in the finite bending regime as well (i.e. $Ca \sim O(1)$). Before we proceed, we would like to make a few points. The mechanism proposed thus far suggests that the primary physics behind vesicle destabilization is curvature change on the interface,

which in turn suggests that the vesicle's initial geometry plays the biggest role in the instability. If this statement is true, we would expect similar shape transitions to occur if we apply a different set of forces on the membrane (such as gravity, electric forces, etc.). In fact, Vlahovska and coworkers have observed a similar set of shape transitions when they places vesicles in an AC electric field (P. M. Vlahovska, private communication, 2013). Similarly, Viallat and coworkers observe pear-shaped transitions when they allow vesicles to settle under the force of gravity (see Huang, Abkarian & Viallat (2011) for experiments and Boedec, Jaeger & Leonetti (2012) for simulations). Lastly, it appears that membrane incompressibility plays a large role in the shape transitions, as similar transitions were observed for droplets, but only in the case when surfactants are strongly adsorbed to the interface, creating a nearly incompressible membrane (Janssen *et al.* 1997; Hu *et al.* 2000). One hypothesis is that surface incompressibility admits particle geometries that otherwise could not be achieved for a simple droplet, and these geometries allow the membrane to be destabilized by curvature changes on the interface. In the future, it is important to understand the role that non-zero compressibility plays in this shape transition.

Lastly, we would like to highlight a few subtle differences between the shape instability and the Rayleigh–Plateau instability. In the classic Rayleigh–Plateau instability, the surface tension is a constant value, which is a material property of the interface and the surrounding fluid. In our situation, the tension is a spatially varying field that depends on the external flow and the base-state geometry. Thus, the curvature-induced pressure depends *indirectly* on the external forces via the extensional flow, which is not the case for the standard theory. Furthermore, there are other competing factors influencing the stability of our system, such as energy contributions from pressure, surface tension and bending. In the next section, we will see that at finite Ca, the membrane stability is primarily governed by a competition between bending (stabilizing) and curvature (destabilizing).

3.4. *Finite bending: shapes, growth rates and mechanism of instability*

In this section, we examine the stability of steady-state vesicles with finite bending (i.e. finite Ca). We will structure this section as before. First, we will determine the steady-state shapes of vesicles, and explore the modal structure of shape perturbations. We will then examine the perturbation energies of the most unstable (non-translating) mode, and use this information to determine the mechanism of instability.

In the no-bending limit ($Ca \to \infty$), the steady-state shape of a vesicle is a prolate ellipsoid. Unfortunately, the steady shapes at finite Ca are not so simple, and we have to resort to numerical techniques to find them. The procedure we follow is described in §2.3. We solve the velocity and tension fields around a non-deforming vesicle in extensional flow (i.e. flow (1) in (3.3)), and determine the normal stresses on the vesicle interface: $[[p]] + 2\sigma H + f_B$. Using root-finding, we adjust the shape until this stress balance vanishes, and hence all boundary conditions are satisfied. The shapes we obtain from this method agree well with boundary integral simulations (figure 4). For intermediate-aspect-ratio vesicles ($\nu > 0.65$), the steady-state shapes at low Ca (i.e. low extension rate) are non-convex. As the capillary number increases, the vesicle stretches along the extension axis and becomes more ellipsoidal. For high-aspect-ratio vesicles (figure 4b), the steady-state shapes are qualitatively different. In this situation, the shapes form a central neck which thins as Ca increases. We will examine these low reduced volume vesicles in more detail in §4.

As before, we determine the stability of the steady-state vesicles by perturbing its interface infinitesimally, and characterizing the modal structure of these perturbations.
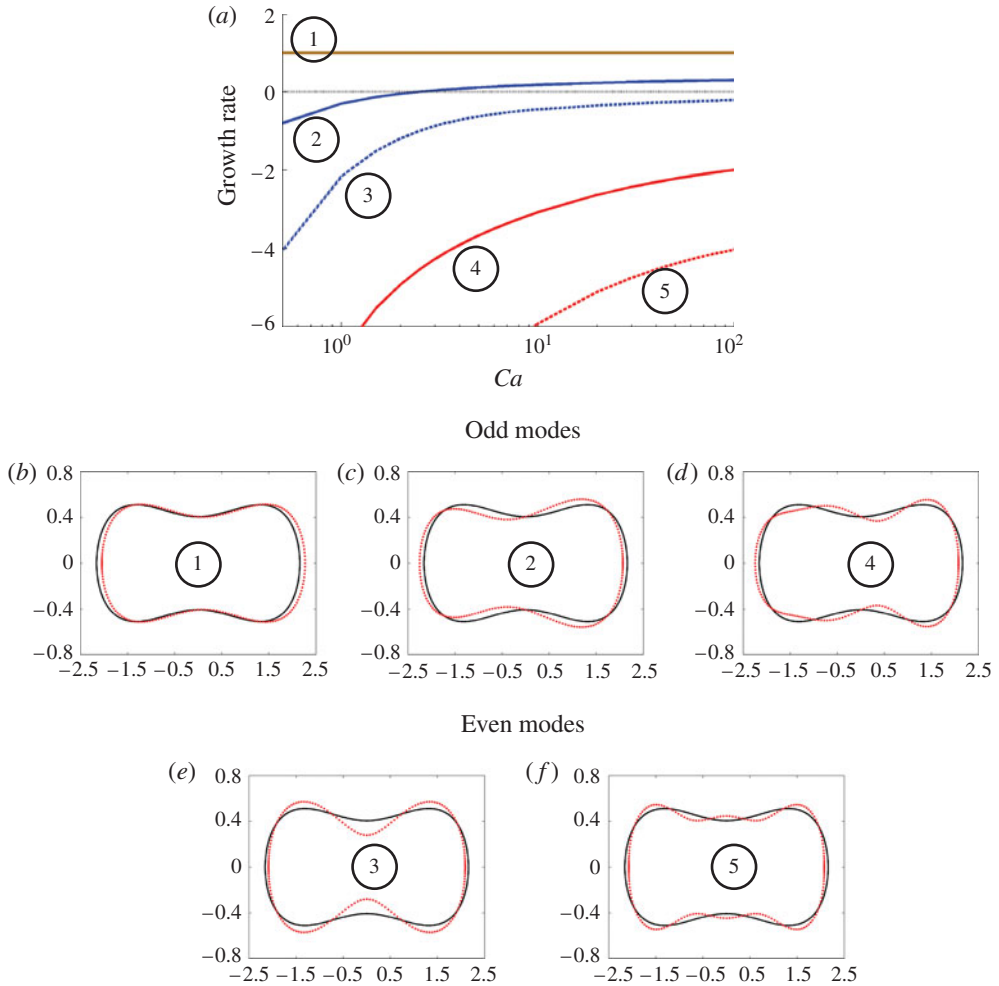
FIGURE 12. (Colour online) Growth rates for intermediate-aspect-ratio vesicles, finite capillary number. (*a*) Plot of the growth rates versus capillary number for the first five deformation modes of the vesicle. The reduced volume is $\nu = 0.65$, and the viscosity ratio is $\lambda = 1$. (*b–f*) The modes at $Ca = 3$. Mode 2 corresponds to the pear-shaped instability observed by Spjut (2010). The shapes are not to scale.

Figure 12 shows the growth rates and shapes of the five most unstable modes of a reduced volume $\nu = 0.65$ vesicle at matched viscosity ratio ($\lambda = 1$). The most unstable mode is translation, while the next mode corresponds to the pear-shaped instability. At low extension rates (low Ca), the pear-shaped mode is stable, while at higher extension rates, the mode is unstable. All other modes (mode 3 onward) appear to be stable to shape perturbations. The third mode looks like 'capillary pinch-off', i.e. formation of a central neck with dumbbell-like ends. The fourth and fifth modes look similar to the pear and pinch-off modes, but with shorter wavelength undulations.

We define the critical capillary number Ca_c for a given mode as the capillary number at which the growth rate becomes zero. In figure 13, we plot Ca_c for the pear-shaped mode as a function of reduced volume, for the two cases of uniaxial flow
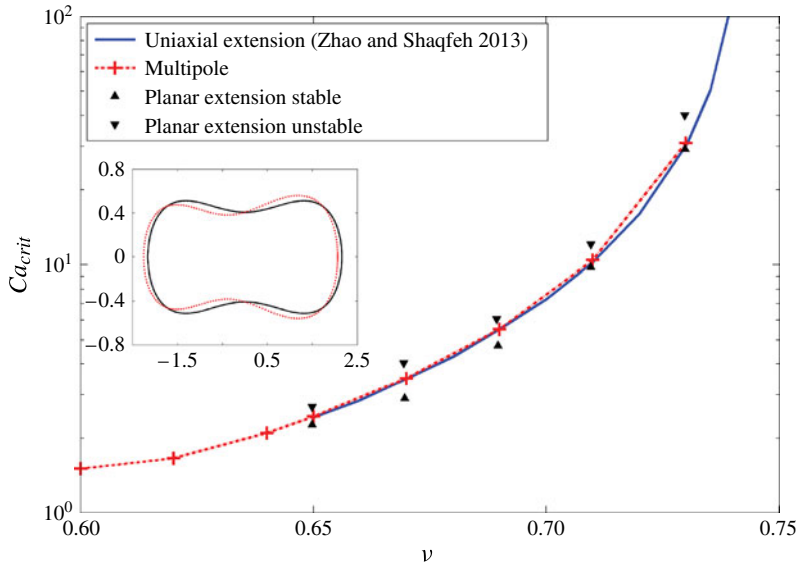
FIGURE 13. (Colour online) Stability boundary, intermediate-aspect-ratio vesicles. We plot the critical capillary number at which the pear-shaped mode (inset) becomes unstable. Our multipole expansion (§ 2.3) agrees well with previous computational studies in uniaxial flow (Zhao & Shaqfeh 2013b). The stability boundary does not appear to change greatly as we modify the flow type to planar extensional flow (at $\lambda = 1$). The critical capillary number increases as the reduced volume increases, with an asymptote at $\nu \approx 0.75$.

and planar extensional flow. This analysis suggests that *flow type does not modify the stability threshold significantly*. We see that Ca_c is $O(1)$ for the reduced volume range $\nu \approx 0.60$–0.65, but starts rapidly increasing after this range, with an asymptote at $\nu = 0.75$. These results agree very well with previous uniaxial boundary integral simulations by Zhao & Shaqfeh (2013b). As proven in § 3.2, the stability threshold in uniaxial extensional flow is independent of the viscosity ratio.

Figure 14 shows the perturbation energies of the pear-shaped mode as a function of capillary number. As before, the convention we use is that positive energies are destabilizing, while negative energies are stabilizing. In this figure, we examine two sets of reduced volumes: one that is always stable to the pear-shaped mode ($\nu = 0.79$), and another that is unstable to the mode at large extension rates ($\nu = 0.65$). For both sets of plots, we find that the pressure contribution to the perturbation energy is negative (stabilizing), while the surface tension contribution is negligible. The curvature energy exhibits different behaviour at different reduced volumes. For reduced volume $\nu = 0.65$, the curvature energy is positive (destabilizing), while at reduced volume $\nu = 0.79$, the curvature energy is negative (stabilizing), but non-monotonic in the capillary number. The bending contribution is for the most part stabilizing, although there is a region of extension rates (i.e. capillary numbers) where it is weakly destabilizing. Nevertheless, the curvature change on the interface plays the biggest role in dictating the stretching transition. Indeed, if we plot the curvature-induced pressure for the two reduced volumes (figure 15), we observe that the pressure profile destabilizes the shape when the curvature energy is positive, but stabilizes the shape when the curvature energy is negative. The takeaway message from this analysis is that *the Rayleigh–Plateau argument is similar in the regime of*
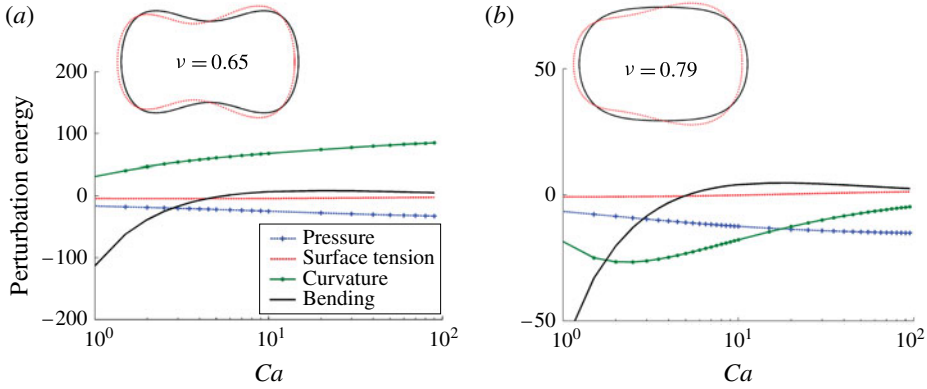
FIGURE 14. (Colour online) Perturbation energies of intermediate-aspect-ratio vesicles, finite *Ca*. Perturbation energies versus capillary number for the pear-shaped mode at reduced volume (*a*) $v = 0.65$ and (*b*) $v = 0.79$. The definitions of the pressure, surface tension, curvature and bending contributions are in (3.7). As the reduced volume decreases (or the aspect ratio increases), the behaviour of the curvature energy changes qualitatively. The convention we employ is that positive energies are destabilizing. For results plotted here, the reference spheroid in our calculations is such that the parameter $cb = 0.475L$, where L is the length of the vesicle.
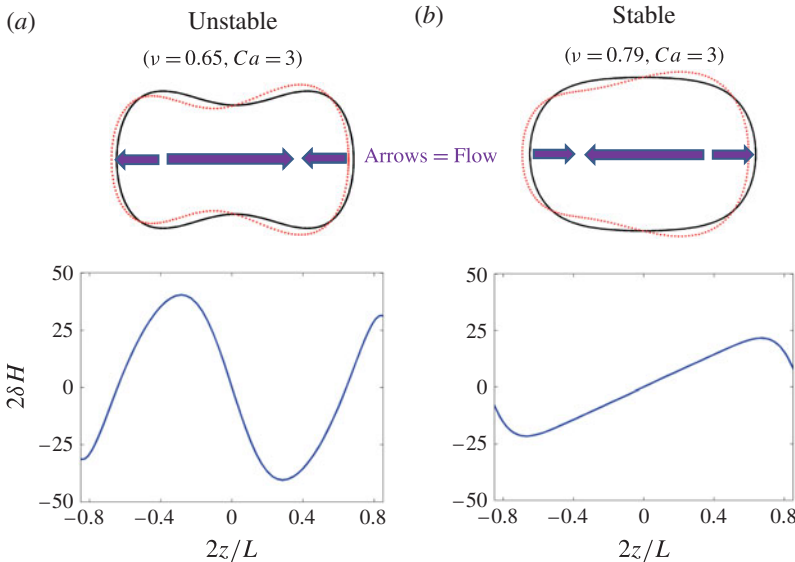

FIGURE 15. (Colour online) Curvature-induced pressures, finite capillary number. We plot the curvature-induced pressures $\delta p = 2\sigma \delta H$ on the interface for the pear-shaped modes shown at the top (solid black line = base-state shape; dotted line (red online) = mode). These curvature pressures induce flows indicated by the arrows (purple online). (*a*) The case when the mode is unstable ($v = 0.65$, $Ca = 3$). (*b*) The case when the mode is stable ($v = 0.79$, $Ca = 3$). The quantity L is the length of the vesicle, with $z = \pm L/2$ corresponding to the ends of the vesicle.

finite bending forces (finite Ca), except that now bending resistance is for the most part an additional stabilizing force.

4. Results: high-aspect-ratio vesicles

In this section, we describe the shape transitions of high-aspect-ratio vesicles in extensional flows, which correspond to the experimental observations found in Kantsler *et al.* (2008*a*). We first examine the steady-state shapes, and then determine what physical processes destabilize the interface, allowing the vesicle to extend without bound in a seemingly symmetric fashion (figure 1*b*). In §4.2, we quantify the critical extension rates for this shape transition, and find that our results agree reasonably well with available experiments (Kantsler *et al.* 2008*a*). In the last section (§4.3), we offer a physical explanation for the pearling phenomenon observed in experiments, which is when a dumbbell-like vesicle forms a series of beads in its central neck. We also offer a simplified theory to predict the stability criterion and the size of the pearls.

4.1. *Steady-state shapes and growth rates of modes*

Figure 4(*b*) plots the steady-state shapes of high-aspect-ratio ($v < 0.57$) vesicles for a wide variety of extensional rates (i.e. *Ca*). At these reduced volumes, the vesicle takes the form of a dumbbell, whose central neck thins with increasing extension rate (*Ca*). We define the aspect ratio for these steady-shapes as the vesicle length divided by its neck diameter, and we plot this value for a $v = 0.40$ vesicle as a function of capillary number in figure 16(*a*). One observation from this plot is that the vesicle deforms rapidly in a narrow range of capillary numbers, so rapidly that we cannot resolve a steady-state shape beyond a critical extension rate. Above this critical capillary number, our boundary integral simulations demonstrate that the vesicle elongates indefinitely, in a fashion similar to the shape transitions observed by Kantsler *et al.* (2008*a*) and the capillary breakup of droplets (see supplementary movies 1 and 2 available at http://dx.doi.org/10.1017/jfm.2014.248). We note in our simulations that the vesicle's membrane remains incompressible after this stretching transition, even if the neck radii is extremely small ($r_{neck} \approx 0.05$). We believe that vesicles in experiments will extend indefinitely at constant area until the central neck becomes small enough that the vesicle lyses (due to the membrane tension becoming exceedingly large). Unfortunately, the experiments by Kantsler *et al.* (2008*a*) do not observe the vesicles for times long enough to offer insight into the long-time behaviour of these particles. Interestingly, if the vesicles extend indefinitely, we would expect the extensional viscosity of a vesicle suspension to increase greatly, as this quantity typically scales as the cube of the particle length for slender bodies.

Figure 16(*b*) plots the steady-state aspect ratios of vesicles for a wide range of reduced volumes. When the reduced volume is above $v = 0.65$, the vesicles become more ellipsoidal with increasing extension rate (see figure 4*a*), which makes the aspect ratio vary weakly with *Ca*. In this situation (i.e. the vesicles studied in §3), a steady-state shape exists at all extension rates. When the reduced volume is below $v = 0.60$, the vesicle's central neck thins rapidly during extension (figure 4*b*), which leads to the aspect ratio diverging at a critical capillary number. To quantify the nature of this critical point, we examine the relative extension of the vesicle, defined as $L^* = L/L_0 - 1$, where L_0 is the no-flow ($Ca = 0$) length of a vesicle. We plot this value versus a normalized capillary number, defined as $1 - Ca/Ca_{crit}$, for a range of reduced volumes ($0.3 < v < 0.49$). We see that the relative extension diverges like a power-law as $Ca \rightarrow Ca_{crit}$, with a best-fit exponent of $\alpha = -0.4$ (figure 16*c*). This power-law behaves
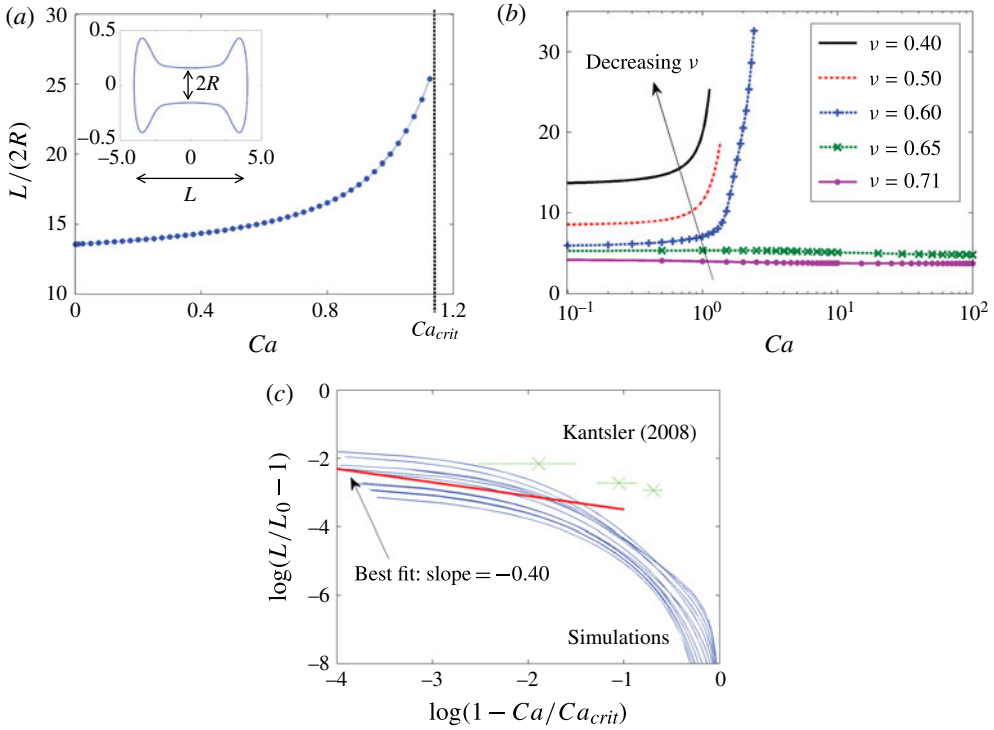
FIGURE 16. (Colour online) Deformation of low-reduced-volume vesicles. (*a*) The steady-state aspect ratio of a $\nu = 0.4$ vesicle as a function of capillary number. We define the aspect ratio $L/(2R)$ as the vesicle length divided by the neck diameter, as shown in the inset. The aspect ratio increases rapidly with Ca until we reach a critical capillary number, beyond which we observe no steady-state solution. (*b*) Aspect ratio versus Ca for a wide variety of reduced volumes. The aspect ratio varies slowly with Ca for intermediate reduced volumes ($\nu > 0.65$), but appears to diverge with Ca for low reduced volumes ($\nu < 0.60$). (*c*) Steady-state extension of vesicle. The curves (blue online) are the relative extensions of vesicles with reduced volume between $0.30 < \nu < 0.49$ (which corresponds to initial aspect ratios between $8.9 < L_0/(2R_0) < 24.5$). The line (red online) is the best-fit power law and the crosses (green online) are experimental measurements by Kantsler *et al.* (2008*a*). We see that the vesicle extension apparently diverges at the critical capillary number with a best fit slope of $(1 - Ca/Ca_{crit})^{-0.4}$.

differently than the coil–stretch transition of polymers ($\alpha = -0.5$) (de Gennes 1974), although there is significant scatter in the simulations and experimental measurements. A more thorough study should be conducted in the future to understand the nature of this critical point better.

As in § 3, we explore the modal structure of shape perturbations around a steady-state vesicle shape. Figure 17 plots the growth rates and shapes of the three most unstable modes of a reduced volume $\nu = 0.40$ vesicle at matched viscosity ratio ($\lambda = 1$). The most unstable mode is translation, while the next mode is an asymmetric perturbation that increases the size of one of the dumbbell lobes. The third mode is the standard capillary pinch-off, i.e. symmetric elongation and thinning of the dumbbell. The second and third modes are stable until we reach the critical capillary number, which is the extension rate beyond which we observe no steady-state
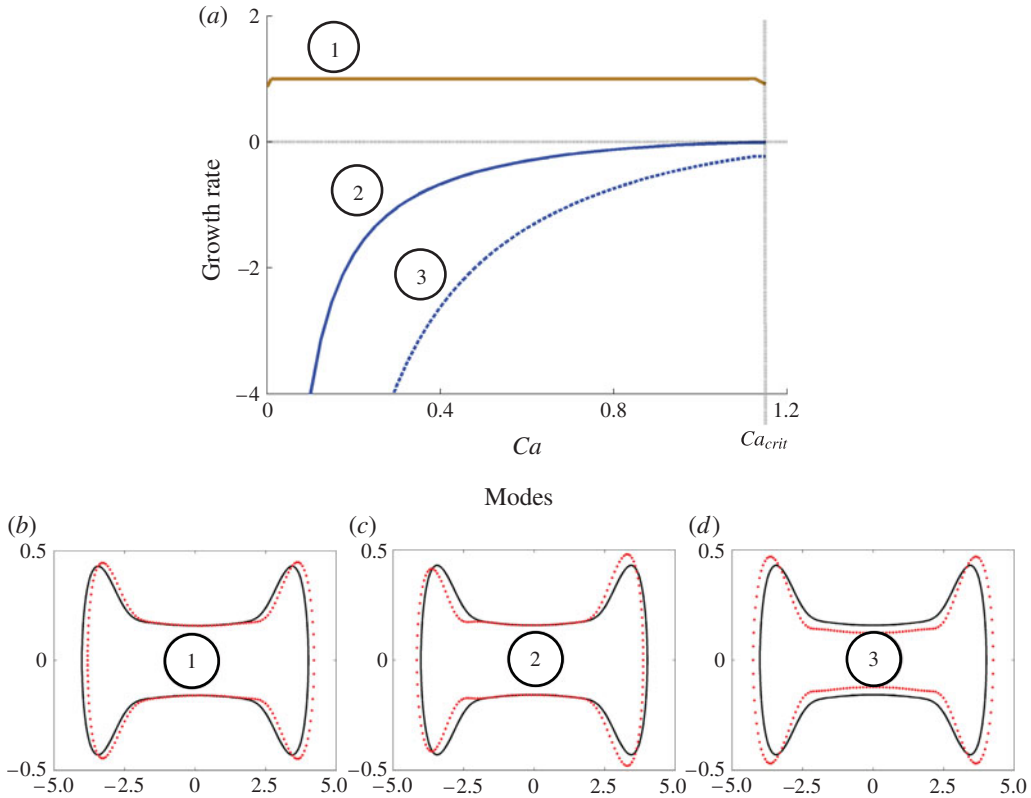
FIGURE 17. (Colour online) Growth rates, high-aspect-ratio particles. (*a*) Plot of the growth rates versus capillary number for the first three deformation modes of the vesicle. The reduced volume is $\nu = 0.40$, and the viscosity ratio is $\lambda = 1$. (*b–d*) The modes at $Ca = 1.125$. When the capillary number reaches Ca_{crit}, the growth rate of mode 2 is nearly zero and the vesicle no longer has a steady state above this extension rate. We believe mode 2 corresponds to the 'burst' instability observed by Kantsler *et al.* (2008*a*) (figure 1*b*). As mode 2 extends indefinitely, any asymmetry in the shape becomes barely noticeable (see figure 18). The shapes above are not to scale.

shape. At this critical *Ca*, the growth rate of the asymmetric mode (mode 2) is nearly zero, which indicates that this mode corresponds to the shape transitions by Kantsler *et al.* (2008*a*). At first glance, this result appears inconsistent with the experiments, as the experimental shape transitions appear symmetric. However, if we look closely at Kantsler's experiments (see time 1.0 and 1.5 in figure 1*b*), we see that the *initial* perturbation is asymmetric, and the shape evolves to a symmetric state as time progresses well past the instability. We observe the same phenomenon in our simulations (figure 18). Many times, the asymmetric perturbation is difficult to visualize, so the casual observer only sees symmetric transitions.

To determine the physical mechanism of the instability, we plot perturbation energies for the asymmetric mode (mode 2) as a function of capillary number (see figure 19). As before, the pressure and bending contributions are stabilizing (negative), while the surface tension contribution is negligible. The curvature energy is stabilizing at low extension rates, but becomes destabilizing (positive) as the extension rate increases, almost balancing all other energy contributions at the critical
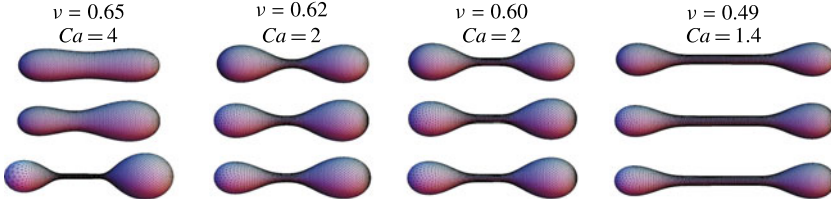
FIGURE 18. (Colour online) Snapshots of odd mode instability. We add an asymmetric perturbation to a steady-state vesicle, and allow the shape to evolve past the instability. As the aspect ratio of the vesicle increases, the asymmetric perturbation becomes less noticeable, and the vesicle stretching appears to be more symmetric. (Reproduced with permission from Spann *et al.* (2014).)
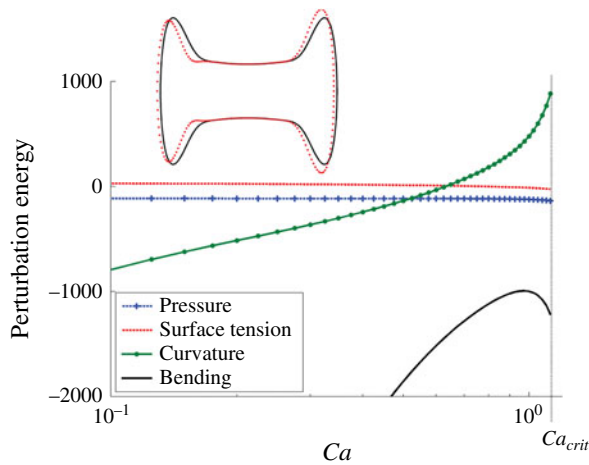

FIGURE 19. (Colour online) Perturbation energies, high-aspect-ratio particles. Perturbation energies versus capillary number for the asymmetric mode (inset) at reduced volume $v = 0.40$. The definitions of the pressure, surface tension, curvature and bending contributions are in (3.7). The convention we employ is that positive energies are destabilizing. The curvature energy rapidly destabilizes near the critical capillary number Ca_{crit}, which is the extension rate beyond which we no longer observe a steady state. For results plotted here, the reference spheroid in our calculations is such that the parameter $cb = 0.475L$, where L is the length of the vesicle.

capillary number where the steady shapes are no longer stable. We find that the curvature energy varies rapidly in the region close to this critical transition, probably due to the fact that the vesicle's aspect ratio varies rapidly as well. This analysis suggests that like before, curvature changes on the interface play the biggest role in destabilizing vesicle shapes. These curvature-induced instabilities are similar to the Rayleigh–Plateau phenomenon discussed in § 3.3.

4.2. *Comparison with experiments: stability boundary*

In this section, we plot the stability boundary for the asymmetric mode (mode 2), and compare these results to the experimental measurements by Kantsler *et al.* (2008*a*). The experiments measure the critical extension rate $\dot{\epsilon}_c$ as a function of the initial
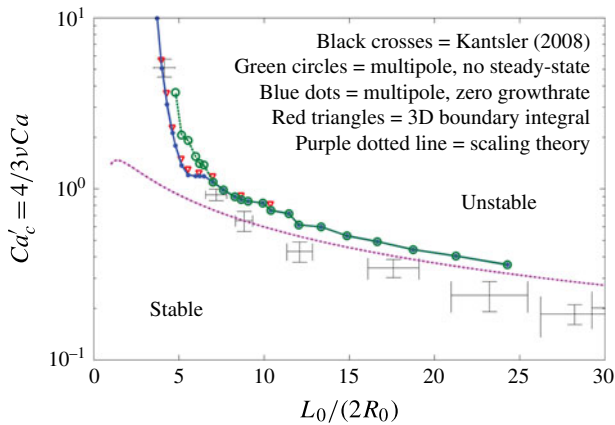
FIGURE 20. (Colour online) Comparison with experiments, burst instability. The black crosses are experimental measurements by Kantsler *et al.* (2008*a*), which correspond to the extension rates at which the vesicle starts to stretch indefinitely like in figure 1. The dots (blue online) and circles (green online) are the simulation results from our multipole expansion (§ 2.3). The dots are capillary numbers at which the asymmetric mode has zero growth rate, while the circles are capillary numbers beyond which we observe no-steady state shape. At high aspect ratios, these two transitions are indistinguishable, but at intermediate aspect ratios, these transitions bifurcate. The triangles (red online) are the stability boundary predicted from our 3D boundary integral simulations. The curve (purple online) is the scaling theory $Ca'_c = C \ln(L/R)/(L/R)$ for $L/R \gg 1$. We choose $C = 4$, as this scaling represents the case when the tensions at the vesicle ends are vanishingly small compared to the values at its centre. See § A.5.1 for derivation.

aspect ratio $L_0/(2R_0)$ of the vesicle (i.e. the equilibrium aspect ratio when $Ca = 0$). The quantity L_0 is the vesicle length, and $R_0 = \sqrt{V/(\pi L_0)}$ is the radius (assuming a cylindrical geometry). Kantsler non-dimensionalizes the extension rates by a time scale $t_{cap} = R_0^2 L_0 \mu_{out}/\kappa$, which yields a critical capillary number $Ca'_c = \frac{4}{3}\nu Ca$. In figure 20, we plot the critical capillary number Ca'_c as a function of the aspect ratio $L_0/(2R_0)$. The black crosses are the experimental measurements by Kantsler *et al.* (2008*a*), which correspond to the extension rates at which the vesicle starts to stretch indefinitely as in figure 1. The dots (blue online) and circles (green online) are the simulation results from our multipole expansion (§ 2.3). The dots are capillary numbers at which the asymmetric mode (mode 2) has zero growth rate, while the circles are capillary numbers beyond which we observe no steady-state shape. At high aspect ratios, these two transitions are the same, but at intermediate aspect ratios, these transitions are distinct. In the intermediate aspect-ratio limit ($3 < L_0/(2R_0) < 7$), the lower curve (dots, blue online) corresponds to the pear-shaped instability which describes the shape transitions observed by Spjut (2010). The upper curve (no steady-state) is most likely not observed in practice. The triangles are results from our 3D boundary integral simulations (§ 2.4). These simulations do not distinguish the type of instability (no steady state versus zero growth rate), but merely indicate when the vesicle first becomes unstable. We find that the stability boundary from our simulations varies slowly at high aspect ratios, but varies very rapidly when the aspect ratio is between 3 and 7. Kantsler states that they cannot observe an instability at aspect ratios below 4.2, which is reasonably close to the asymptote our simulations predict (approximately 3). In general, the boundary integral and multipole simulations

agree reasonably well with experiments, although our simulations slightly overestimate the critical extension rates. There can be many reasons for this slight discrepancy, but we feel the most likely choice is that Kantsler used an order-of-magnitude estimate of the vesicle bending modulus, which is 20 % larger than the values measured in experiments (Rawicz *et al.* 2000; Pan *et al.* 2008). This effect slightly lowers Kantsler's critical capillary number, which is consistent with the results in figure 20. Our simulations also neglect fluctuations of the membrane, which could be important near the critical transition. Indeed, Kantsler *et al.* (2008*a*) observes significant fluctuations in the vesicle's relative extension (i.e. $L^* = L/L_0 - 1$) near this critical region (see figure 3 in paper). Note that in this study, we explore a much wider range of aspect ratios than in previous computational works (Spann 2013; Zhao & Shaqfeh 2013*b*).

Following the discussion of Kantsler *et al.* (2008*a*), we can develop a simple scaling argument to predict how the stability boundary varies with aspect ratio when this quantity is large. In this regime, vesicles are nearly cylindrical with a length L and radius R. The bending pressure at the interface thus scales as κ/R^3, and the capillary pressure scales as σ/R, where κ is the bending modulus of the interface, and σ is the surface tension. We expect an instability to occur when the capillary forces overcome bending resistance, i.e. $\sigma/R > \kappa/R^3$. From the interfacial force balance (2.4), we see that surface tension gradients balance the tangential stresses on the interface, so $\sigma/L \sim T_{rz} \sim \mu_{out}\dot{\epsilon}L/(R\ln(L/R))$ as predicted by slender body theory (Batchelor 1970). Combining these statements yields the criterion $Ca'_c > C\ln(L/R)/(L/R)$ for instability, where C is an $O(1)$ constant which must be determined by numerically solving the Stokes flow around the vesicle. We choose not to perform this task, but instead estimate this constant using a simpler procedure. We assume the vesicle is a steady-state cylinder in extensional flow, with no tension on its ends. We solve for the capillary forces on the interface, and determine when the maximum value of these forces exceeds the bending resistance. This analysis yields $C = 4$, which agrees surprisingly well with Kantsler's experiments at large aspect ratio (see figure 20, dotted curve, purple online). We note that Kantsler does the same analysis as performed here, but appears to determine the constant C by fitting, rather than offering a detailed analysis for what the constant should be. For more details on the scaling theory, see §A.5.1.

In the next section, we discuss the physical origin of the pearling phenomenon, which is the second set of shape transitions observed by Kantsler *et al.* (2008*a*).

4.3. *Physical mechanism of pearling*

When a high-aspect-ratio vesicle is beyond the critical capillary number described in the previous section, the vesicle starts to extend indefinitely, creating a central neck that thins continuously in time. If the extension rate is large enough (characterized by another critical condition), the thinning neck eventually creates pearls, which are periodic beads in the central thread (see figure 1*b*, time 3.0 onwards). These shapes are similar to those found in the capillary breakup of a liquid column, which is described by the Rayleigh–Plateau instability (Tomotika 1935). We can use this same framework to describe the shape transitions of a pearling vesicle, as shown below.

When a vesicle thins continuously in time, its aspect ratio becomes very large, and hence its shape becomes nearly cylindrical. Furthermore, the stresses vary slowly along the interface (at least on the length scale of the neck's radius), so we can locally treat the neck as an infinite cylinder of radius R with constant surface tension σ.
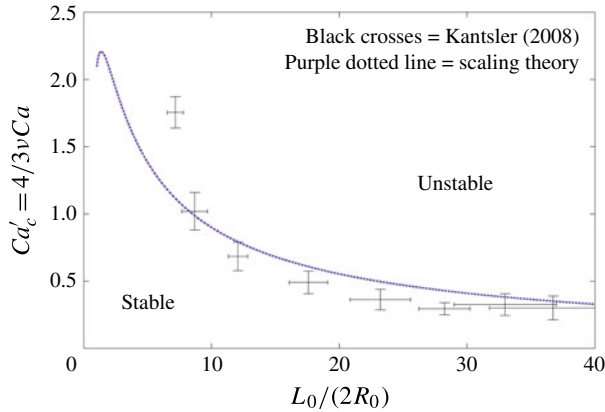
FIGURE 21. (Colour online) Comparison with experiments, pearling instability. The black crosses are experimental measurements by Kantsler *et al.* (2008*a*), which correspond to the extension rates at which the vesicle starts to pearl. The curve (purple online) is the scaling theory $Ca'_c = C \ln(L/R)/(L/R)$ for $L/R \gg 1$. We choose $C = 6$, as this scaling represents the case when the tensions at the vesicle ends are vanishingly small compared with the values at its centre. See § A.5.2 for derivation.

We determine the conditions under which this configuration is unstable by examining the free energy of the interface, which consists of bending, surface tension and pressure. Instead of performing the full variational analysis, we examine the simpler case of perturbing the interface by a constant radius δR, where $|\delta R| \ll R$, as this procedure gives the same stability limits as the full analysis (see § A.6). The free energy expansion per unit length is

$$E = \frac{\pi\kappa}{R} + 2\pi R(\delta R)\left[\frac{\sigma}{R} - \frac{\kappa}{2R^3} + \Delta p\right] + \pi R(\delta R)^2\left[\frac{\kappa}{R^4} + \frac{\Delta p}{R}\right] + O(\delta R^3) \qquad (4.1)$$

where Δp is the pressure jump across the interface (outer minus inner). The first variation of this energy with respect to δR gives a constraint on the pressure jump which is exactly the normal component of the stress balance: $\Delta p = -\sigma/R + \kappa/(2R^3)$. The second variation determines whether the base-state shape is at a local energy minimum, and hence stable. We find that a cylinder is unstable to shape perturbations if the surface tension is above a critical value $\sigma_c = 3\kappa/(2R^2)$, which is a remarkably simple *local* stability criterion for pearling.

Because the critical surface tension scales as κ/R^2, we expect the critical capillary number for the pearling transition to have the same scaling as in the previous section: $Ca'_c = C \ln(L/R)/(L/R)$, where C is an $O(1)$ constant. As before, we estimate this constant by assuming the vesicle is a cylinder in extensional flow, with no tension at its ends. However, in this situation, the cylinder's radius is also decreasing in time, since the vesicle's neck is rapidly thinning. We solve for the surface tension distribution on the vesicle, and determine when the maximum value exceeds the critical condition $\sigma_c = 3\kappa/(2R^2)$. This analysis, performed in § A.5.2, yields the constant $C = 6$. In figure 21, we plot the results of this scaling analysis, and compare it with the data of Kantsler *et al.* (2008*a*) when they first observe the pearling transition. We find that our scaling theory again agrees well with the experimental data.
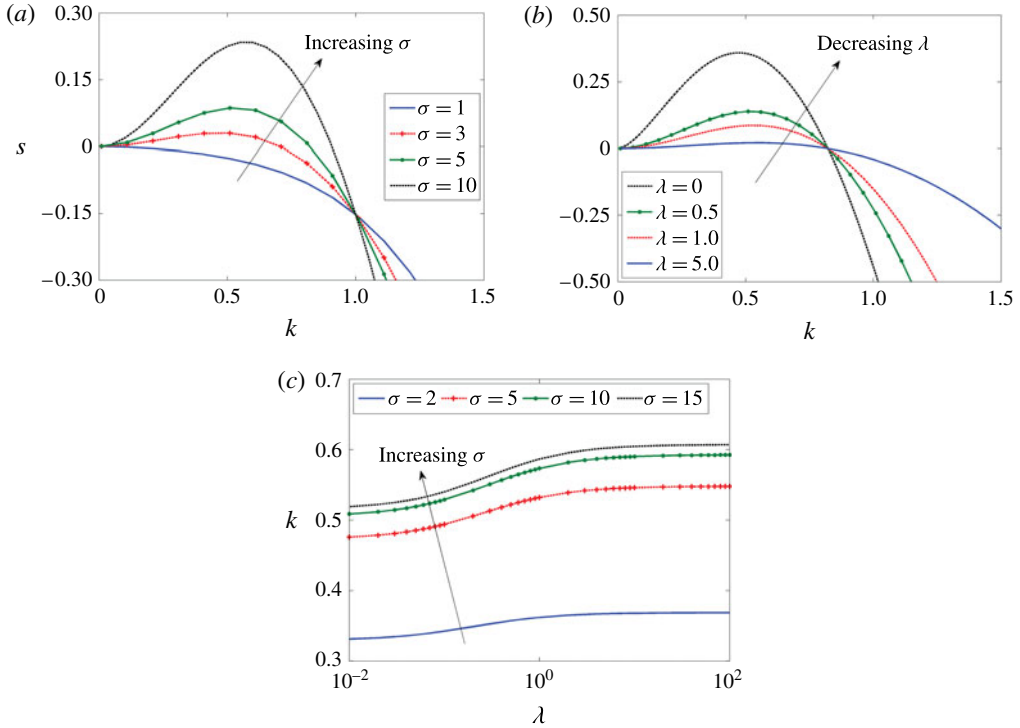
FIGURE 22. (Colour online) Growth rates, pearling instability. We examine the stability of an infinitely long, cylindrical vesicle to infinitesimal perturbations to its interface. (*a*, *b*) Plots of the growth rate *s* versus the perturbation wavenumber *k*: (*a*) examination of the dependence of *s* on the applied tension σ; (*b*) examination of the dependence of *s* on the viscosity ratio λ. (*c*) Plot of the most unstable wavenumber (i.e. wavenumber selection) as a function of viscosity ratio and applied tension. For these figures, we non-dimensionalize growth rates by $\kappa/(\mu_{out}R^3)$, tensions by κ/R^2, and wavenumbers by R^{-1}, where R is the radius of the cylinder. In (*a*), the viscosity ratio is $\lambda = 1$, while in (*b*), the tension is $\sigma = 5$.

To obtain the local growth rates of the pearling modes, we perform a linear stability analysis on an infinite cylinder with prescribed surface tension σ and bending modulus κ. This analysis is not novel, as it has been performed many times in the literature (Goldstein *et al.* 1996; Powers 2010), with the latest (and most accurate version) by Boedec, Jaeger & Leonetti (2014). We outline a simplified derivation of the dispersion relationship in §A.6, and plot the growth rates in figure 22(*a,b*). We observe that pearling only occurs for long-wavelength perturbations ($kR < 1$), as long as the surface tension is beyond the critical condition $\sigma > \sigma_c \equiv 3\kappa/(2R^2)$. We can explain this phenomenon using the same arguments in the previous sections, i.e. curvature changes on the interface destabilize the membrane. If we apply a small sinusoidal perturbation $\delta R \cos(kz)$ to a membrane with a background tension σ, the curvature-induced pressure increases by $\delta p_{curv} \sim \sigma[1 - (kR)^2]\delta R/R^2$ in the regions pinched by the perturbation. However, bending stabilizes these regions by decreasing the pressure by $\delta p_{bend} \sim \kappa[(kR)^2/2 - (kR)^4 - 3/2]\delta R/R^4$. When the surface tension is above the critical condition ($\sigma > \sigma_c$), the curvature-induced pressure dominates, and long-wavenumber perturbations ($kR < 1$) create pearls by generating a leakage

flux away from the pinched regions. From the growth rates plotted in figure 22, we see that the size of the pearls will be slightly larger than the neck's radius R. The wavenumber corresponding to maximum growth varies modestly with the applied tension σ and viscosity ratio λ, increasing as both of these quantities increase (figure 22c).

Before we conclude, we would like to highlight several differences between pearling for vesicle systems and droplets. Droplets rarely go through the pearling transition during flow, but form pearls after flow cessation (Stone 1994). Vesicles, on the other hand, do not pearl if the flow rate is turned off, provided that the initial extension rate is below the critical values indicated by figure 21 (Kantsler *et al.* 2008a). We believe that the vesicle's membrane incompressibility plays a large role in preventing these transitions. For the vesicle system, the pearling phenomenon is controlled by the surface tension in the thread (i.e. $\sigma > \sigma_c$), which in turn is governed by the external flow due to surface incompressibility. When flow is turned off, the tension decreases, which stabilizes the thread. For the droplet system, this stabilization mechanism does not occur, as the surface tension is a material property independent of the flow. We also note that Kantsler *et al.* (2008a) does not observe tip streaming, i.e. when satellite beads eject from the ends of the vesicle. This transition occurs when the ends of the particle are sharp like a cusp, which is highly unlikely to occur for vesicle systems due to the bending resistance of the interface.

5. Conclusions and future directions

In this paper, we describe the physics behind the shape transitions of vesicles in extensional flows. At intermediate aspect ratios (reduced volume $\nu \geqslant 0.65$), we find that the particles stretches to an asymmetric dumbbell, while at higher aspect ratios ($\nu < 0.6$), the particle extends without bound in a seemingly symmetric fashion, similar to the capillary breakup of droplets. We find the physical mechanism for shape destabilization to be similar for these two cases. When the vesicle's shape is subject to an *asymmetric* perturbation, the membrane's change in curvature generates a flow field in the interior of the particle that amplifies the perturbation at sufficiently high extension rates. We quantify the conditions under which the vesicle becomes unstable, and we find that the stability boundary calculated by our simulations agrees well with available experimental data (figure 20). We also examine the pearling phenomenon, i.e. when a rapidly thinning vesicle creates a series of beads in its central neck. We develop a scaling theory to predict the onset of pearling, as well as the growth rate and size of the pearls. The scaling theory, which is simple, agrees reasonably well with available experiments (figure 21).

We note that the physical mechanism behind the shape transitions is *remarkably similar to the Rayleigh–Plateau phenomenon*, which describes the curvature-induced destabilization of an interface. This analysis suggests that the vesicle's initial geometry plays the largest role in the shape transitions under tension, regardless of what type of force is applied (i.e. hydrodynamic, electrical, etc.). In fact, Vlahovska and coworkers observe similar set of dumbbell-like shapes when they place vesicles in an AC electric field (P. M. Vlahovska, private communication, 2013). A natural extension would be to thus use the same mathematical machinery in this paper to understand the stability of vesicles under electrical forces. Note that previous studies have used spheroidal coordinates to model the dynamics of vesicles in electric fields, but these studies did not examine the instability observed by Vlahovska, and they assumed a spheroid shape throughout the vesicle motion (Zhang *et al.* 2013). From an experimental standpoint, it is much easier to manipulate biological particles (such as vesicles) under electric forces than hydrodynamic forces.

We hope this paper will be helpful in understanding the dynamics of vesicles under strong tension, and thus provide insight into the design of these particles for future biomedical applications. In the future, it is important to see whether the effects described in this paper occur for a wider range of biological particles enclosed by phospholipid membranes, such as cells.

Acknowledgements

Supplementary movie

Supplementary movie is available at http://dx.doi.org/10.1017/jfm.2014.248.

Appendix

A.1. *Legendre functions*

We define $P_n(x)$ and $Q_n(x)$ as Legendre functions of the first and second kind, which are the linearly independent solutions to the differential equation:

$$\frac{\mathrm{d}}{\mathrm{d}x}\left((1-x^2)\frac{\mathrm{d}y}{\mathrm{d}x}\right) + n(n+1)y = 0. \tag{A 1}$$

The Legendre function $P_n(x)$ is regular everywhere except infinity, while the Legendre function $Q_n(x)$ is regular everywhere except $x = \pm 1$. The first few terms of these functions are

$$\left.\begin{aligned}
P_0(x) &= 1 & P_1(x) &= x \\
Q_0(x) &= \frac{1}{2}\ln\left|\frac{1+x}{x-1}\right| & Q_1(x) &= \frac{x}{2}\ln\left|\frac{1+x}{x-1}\right| - 1 \\
P_{n+1}(x) &= \frac{2n+1}{n+1}xP_n(x) - \frac{n}{n+1}P_{n-1}(x) \\
Q_{n+1}(x) &= \frac{2n+1}{n+1}xQ_n(x) - \frac{n}{n+1}Q_{n-1}(x).
\end{aligned}\right\} \tag{A 2}$$

We note that the recursion relation is the same for both types of Legendre functions. Their asymptotic behaviour as $x \to \infty$ is

$$P_n(x) \to \frac{(2n-1)!!}{n!}x^n \quad \text{as } x \to \infty \tag{A 3a}$$

$$Q_n(x) \to \frac{n!}{(2n+1)!!}x^{-n-1} \quad \text{as } x \to \infty \tag{A 3b}$$

where !! is the double factorial function (i.e. $(2n+1)!! = (2n+1) \times (2n-1) \times \cdots \times 3 \times 1$). Another important recursion relation for the derivatives of these functions is

$$(2n+1)(1-x^2)P_n'(x) = n(n+1)(P_{n-1}(x) - P_{n+1}(x)). \tag{A 4}$$

As before, this recurrence relation holds for $Q_n(x)$ as well.

From Sturm–Liouville theory, the Legendre functions $P_n(x)$ form a complete, orthogonal set of functions in the domain $|x| \leqslant 1$. Thus, any bounded function in $|x| \leqslant 1$ can be expressed as a linear combination of $P_n(x)$. The orthogonality relationship between Legendre polynomials is

$$\langle P_n(x), P_m(x) \rangle = \int_{-1}^{1} P_n(x) P_m(x) \, \mathrm{d}x = \frac{2}{2n+1} \delta_{nm}, \qquad (A\,5)$$

where δ_{nm} is the Kronecker delta ($\delta_{ij} = 1$ when $i = j$ and zero otherwise).

We numerically evaluate Legendre functions $P_n(x)$ using the forward-recursion relation (A 2). For $Q_n(x)$, we employ the same recursion relation, but iterate backwards from a large value of n, as this process is numerically stable (Abramowitz & Stegun 1972). We evaluate $Q_n(x)$ for large n by expressing it in terms of hypergeometric functions, which are straightforward to evaluate (Abramowitz & Stegun 1972).

A.2. *Derivation of multipole solution*

A.2.1. *Gradient operator in spheroidal coordinates*

In spheroidal coordinates, the gradient operator is (Hobson 1931)

$$\boldsymbol{\nabla} = \frac{1}{h_\tau} \hat{\boldsymbol{\tau}} \frac{\partial}{\partial \tau} + \frac{1}{h_\xi} \hat{\boldsymbol{\xi}} \frac{\partial}{\partial \xi} + \frac{1}{h_\phi} \hat{\boldsymbol{\phi}} \frac{\partial}{\partial \phi} \qquad (A\,6)$$

where the stretch factors (h_τ, h_ξ, h_ϕ) are

$$h_\tau = \frac{cb\sqrt{\tau^2 - \xi^2}}{\sqrt{\tau^2 - 1}}, \quad h_\xi = -\frac{cb\sqrt{\tau^2 - \xi^2}}{\sqrt{1 - \xi^2}}, \quad h_\phi = cb\sqrt{\tau^2 - 1}\sqrt{1 - \xi^2} \qquad (A\,7a\text{--}c)$$

and the unit vectors are

$$\left. \begin{aligned} \hat{\boldsymbol{\tau}} &= \frac{1}{\sqrt{\tau^2 - \xi^2}} (\tau\sqrt{1 - \xi^2}\cos(\phi), \ \ \tau\sqrt{1 - \xi^2}\sin(\phi), \ \ \xi\sqrt{\tau^2 - 1}) \\ \hat{\boldsymbol{\xi}} &= \frac{1}{\sqrt{\tau^2 - \xi^2}} (\xi\sqrt{\tau^2 - 1}\cos(\phi), \ \ \xi\sqrt{\tau^2 - 1}\sin(\phi), \ \ -\tau\sqrt{1 - \xi^2}) \\ \hat{\boldsymbol{\phi}} &= (-\sin(\phi), \ \ \cos(\phi), \ \ 0). \end{aligned} \right\} \qquad (A\,8)$$

A.2.2. *Derivation of multipole solution*

The Papkovich–Neuber equations state that the solution to Stokes flow is (Tran-Cong & Blake 1982; Dassios *et al.* 2004)

$$\boldsymbol{u} = \boldsymbol{\Phi} - \tfrac{1}{2}\boldsymbol{\nabla}(\boldsymbol{x} \cdot \boldsymbol{\Phi} + \chi), \quad p = -\eta \boldsymbol{\nabla} \cdot \boldsymbol{\Phi}, \qquad (A\,9a,b)$$

where $\boldsymbol{\Phi}$ and χ are harmonic functions, and η is the non-dimensional viscosity of the medium (in our case, $\eta = 1$ outside the vesicle and $\eta = \lambda$ inside the vesicle).

In prolate ellipsoidal coordinates, the growing and decaying harmonics are as follows:

$$\left. \begin{aligned} \textit{Growing}: \quad & S_n^{m,(grow)} = P_n^m(\tau) P_n^m(\xi) \exp(im\phi) \\ \textit{Decaying}: \quad & S_n^{m,(decay)} = Q_n^m(\tau) P_n^m(\xi) \exp(im\phi) \end{aligned} \right\} \qquad (A\,10)$$

where $P_n^m(x)$ and $Q_n^m(x)$ are Legendre functions of the first and second kind (see § A.1). For our problem, we consider the vesicle and shape perturbations to be axisymmetric

about the z axis. Thus, we neglect all ϕ dependence (i.e. set $m = 0$), and choose our harmonic potentials to be

$$
\left.
\begin{aligned}
\chi &= cb^2 \sum_{n=0}^{\infty} d_n R_n(\tau) P_n(\xi) \\
\boldsymbol{\Phi} &= b\hat{\boldsymbol{z}} \sum_{n=0}^{\infty} c_n R_n(\tau) P_n(\xi)
\end{aligned}
\right\}
\tag{A 11}
$$

where $R_n(\tau)$ equals $P_n(\tau)$ for the growing harmonics, and $Q_n(\tau)$ for the decaying harmonics. We substitute these potentials into the Papkovich–Neuber equations (A 9) to obtain the velocity and pressure fields shown below:

$$
u_\tau = \frac{cb^2}{h_\tau} \sum_{n=0}^{\infty} \left[\frac{1}{2} \xi c_n P_n(\xi)(R_n(\tau) - \tau R_n'(\tau)) - \frac{1}{2} d_n P_n(\xi) R_n'(\tau) \right]
\tag{A 12}
$$

$$
u_\xi = -\frac{cb^2}{h_\xi} \sum_{n=0}^{\infty} \left[\frac{1}{2} \tau c_n R_n(\tau)(\xi P_n'(\xi) - P_n(\xi)) + \frac{1}{2} d_n R_n(\tau) P_n'(\xi) \right]
\tag{A 13}
$$

$$
-\frac{p}{\eta} = \frac{1}{c(\tau^2 - \xi^2)} \sum_{n=0}^{\infty} c_n [\xi(\tau^2 - 1)R_n'(\tau)P_n(\xi) + \tau(1 - \xi^2)R_n(\tau)P_n'(\xi)].
\tag{A 14}
$$

Now that we have the velocity and pressure fields, let us determine the stress components. Recall that $\boldsymbol{u} = \boldsymbol{\Phi} - \frac{1}{2}\nabla(\boldsymbol{x} \cdot \boldsymbol{\Phi} + \chi)$ in the Papkovich–Neuber representation (A 9). When $\boldsymbol{\Phi} = \Phi\hat{\boldsymbol{z}}$ as is done here, the deviatoric stress is

$$
\frac{1}{\eta}\boldsymbol{T} = \nabla\boldsymbol{u} + \nabla\boldsymbol{u}^T = -z\nabla\nabla\Phi - \nabla\nabla\chi = -\sum_{n=0}^{\infty}(bc_n z + cb^2 d_n)\nabla\nabla R_n(\tau)P_n(\xi).
\tag{A 15}
$$

Thus, to find the components of the deviatoric stress, we need to determine the components of the double-gradient tensor $\nabla\nabla$. Details of the gradient operator are given in §A.2.1. After some tedious algebra, we find that the components of the deviatoric stress tensor are

$$
\frac{1}{\eta}\boldsymbol{T} = -\sum_{n=0}^{\infty}(c_n c\tau\xi + cd_n)\boldsymbol{L}[R_n(\tau)P_n(\xi)],
\tag{A 16}
$$

where

$$
\left.
\begin{aligned}
L_{\tau\tau} &= \frac{(1-\xi^2)}{c^2(\tau^2-\xi^2)^2}\left(\tau\frac{\partial}{\partial\tau} - \xi\frac{\partial}{\partial\xi}\right) + \frac{\tau^2-1}{c^2(\tau^2-\xi^2)}\frac{\partial^2}{\partial\tau^2} \\
L_{\xi\xi} &= \frac{(\tau^2-1)}{c^2(\tau^2-\xi^2)^2}\left(\tau\frac{\partial}{\partial\tau} - \xi\frac{\partial}{\partial\xi}\right) + \frac{1-\xi^2}{c^2(\tau^2-\xi^2)}\frac{\partial^2}{\partial\xi^2} \\
L_{\phi\phi} &= \frac{1}{c^2(\tau^2-\xi^2)}\left(\tau\frac{\partial}{\partial\tau} - \xi\frac{\partial}{\partial\xi}\right) \\
L_{\tau\xi} = L_{\xi\tau} &= \frac{\sqrt{\tau^2-1}\sqrt{1-\xi^2}}{c^2(\tau^2-\xi^2)^2}\left(\tau\frac{\partial}{\partial\xi} - \xi\frac{\partial}{\partial\tau} - (\tau^2-\xi^2)\frac{\partial^2}{\partial\tau\partial\xi}\right) \\
L_{\tau\phi} = L_{\phi\tau} &= L_{\phi\xi} = L_{\xi\phi} = 0.
\end{aligned}
\right\}
\tag{A 17}
$$

A.3. *Differential geometry of vesicle interface in spheroidal geometry*

A.3.1. *Evaluation of the bending force*

Suppose we have an axisymmetric vesicle in a prolate spheroidal geometry, whose shape is parameterized by the level surface $\tau = g(\xi)$. If we convert to cylindrical coordinates, the position vector $\boldsymbol{x}$ on the interface is

$$\boldsymbol{x}(\xi, \phi) = r(\xi)\hat{\boldsymbol{r}} + z(\xi)\hat{\boldsymbol{z}}, \tag{A 18}$$

where

$$\left.\begin{array}{ll} r(\xi) = cb\sqrt{g^2 - 1}\sqrt{1 - \xi^2} & z(\xi) = cbg\xi \\ \hat{\boldsymbol{r}} = [\cos(\phi), \sin(\phi), 0] & \hat{\boldsymbol{z}} = [0, 0, 1]. \end{array}\right\} \tag{A 19}$$

Given this position vector, we can calculate the metric and curvature tensors and their associated geometrical quantities, such as curvatures and differential areas/volumes. The components of the metric tensor ($\boldsymbol{\Lambda}$) and curvature tensor ($\boldsymbol{B}$) are

$$\Lambda_{pq} = \frac{\partial \boldsymbol{x}}{\partial p} \cdot \frac{\partial \boldsymbol{x}}{\partial q}, \quad B_{pq} = -\boldsymbol{n} \cdot \frac{\partial^2 \boldsymbol{x}}{\partial p \partial q}, \tag{A 20a,b}$$

where p and q are either the surface coordinates ξ or ϕ, and $\boldsymbol{n}$ is the outward-pointing unit normal vector, which is

$$\boldsymbol{n} = \frac{z'\hat{\boldsymbol{r}} - r'\hat{\boldsymbol{z}}}{\sqrt{r'^2 + z'^2}}. \tag{A 21}$$

Given the metric and curvature tensors, the principal curvatures of the interface are the eigenvalues of $\boldsymbol{\Lambda}^{-1} \cdot \boldsymbol{B}$, which are easy to evaluate since both tensors are diagonal for an axisymmetric shape. The mean curvature H is the mean of the two principal curvatures, while the Gaussian curvature K is the product of the two principal curvatures.

To calculate the bending forces on the vesicle, we not only need to calculate the curvatures on the interface, but the *surface Laplacian* of the curvature (see (2.4)). In an axisymmetric geometry, this operator takes a simple form (Veerapaneni *et al.* 2009).

$$\nabla_s^2 H = \frac{1}{J} \left(\frac{\Lambda_{\phi\phi} H'}{J} \right)'. \tag{A 22}$$

In the above equation, J is the differential area of the surface, defined by $J = \sqrt{\det(\Lambda_{pq})}$. We now have all of the information necessary to calculate the bending forces on the interface. We first decompose the vesicle shape $g(\xi)$ into Legendre modes, as described in (2.13), up to a certain cutoff mode M, and evaluate the principal curvatures analytically. In principle, we can calculate $\nabla_s^2 H$ analytically, but in spheroidal coordinates, the algebra is complicated, and thus we employ a central difference approximation instead. In most situations, we only need to calculate one derivative in the central difference scheme, since when we project the bending force onto Legendre modes, we can integrate by parts to get rid of higher-order derivatives.

A.3.2. *Evaluation of kinematic and surface incompressibility boundary conditions*

Let us write the normal ($\boldsymbol{n}$), tangential ($\boldsymbol{t}$), and azimuthal ($\boldsymbol{b}$) vectors in spheroidal coordinates for a vesicle interface parametrized by the level surface $\tau = g(\xi)$:

$$\boldsymbol{n} = \frac{\hat{\boldsymbol{\tau}} - \psi\hat{\boldsymbol{\xi}}}{\sqrt{1 + \psi^2}}, \quad \boldsymbol{t} = \frac{\hat{\boldsymbol{\xi}} + \psi\hat{\boldsymbol{\tau}}}{\sqrt{1 + \psi^2}}, \quad \boldsymbol{b} = \hat{\boldsymbol{\phi}} \quad \text{where } \psi = \frac{h_\tau}{h_\xi} g'(\xi). \tag{A 23a–c}$$

Given these directions, the normal and tangential velocity on the interface is:

$$u_n = \frac{1}{\sqrt{1+\psi^2}}(u_\tau - \psi u_\xi), \quad u_t = \frac{1}{\sqrt{1+\psi^2}}(u_\xi + \psi u_\tau). \qquad (A\,24a,b)$$

In this subsection, we write the kinematic and surface incompressibility boundary conditions in terms of the normal (u_n) and tangential (u_t) velocities. We can relate these boundary conditions to the multipole velocity coefficients $\{c_n, d_n\}$ by converting the normal and tangential velocities into u_τ and u_ξ as shown above, and then use the multipole velocity relations in (2.10) and (2.11).

The kinematic boundary condition is

$$u_n = \frac{\dfrac{\partial g}{\partial t}}{\|\nabla(\tau - g)\|} = \frac{h_\tau}{\sqrt{1+\psi^2}}\frac{\partial g}{\partial t}. \qquad (A\,25)$$

To derive the incompressibility boundary condition, we decompose the velocity field on the interface into normal (u_n) and tangential (u_t) components, and rewrite the boundary condition in terms of these fields: $\nabla_s \cdot \mathbf{u} = 2Hu_n + \nabla_s \cdot (u_t\mathbf{t}) = 0$. For an axisymmetric vector field that lies entirely on the surface of the interface, such as $u_t\mathbf{t}$, the surface divergence takes a particularly simple form:

$$\nabla_s \cdot \mathbf{a} = -\frac{1}{J}\frac{\mathrm{d}}{\mathrm{d}\xi}(\sqrt{\Lambda_{\phi\phi}}\,a_t), \qquad (A\,26)$$

where $\Lambda_{\phi\phi}$ is $\phi\phi$ component of the metric tensor (A 20), and $J = \sqrt{\det(\Lambda_{pq})}$ is the differential area. Substituting these expressions, we find that the surface incompressibility boundary condition is

$$2HJu_n = \frac{\mathrm{d}}{\mathrm{d}\xi}(h_\phi u_t). \qquad (A\,27)$$

When we project this equation onto the set of Legendre modes, we typically remove the derivatives on the right-hand side via integration by parts.

A.4. *Shape and tensions of vesicle with no bending in uniaxial extensional flow*

A vesicle in uniaxial flow is a prolate spheroid at steady state, provided that the reduced volume is not too small ($v > 0.67$) and the interface has no bending resistance. We will prove this fact by assuming the vesicle is a prolate spheroid, and show that such a shape satisfies the Stokes equations with zero normal velocity at the interface. We parameterize the vesicle shape in spheroidal coordinates, with the reference ellipsoid coinciding exactly with the vesicle's interface. With this choice of coordinate system, the vesicle's surface is a surface of constant τ, with $\tau = \tau^* = \sqrt{1+1/c^2}$. The value of c is the product between the vesicle's aspect ratio and eccentricity.

Let us solve for the velocity field around the vesicle. In spheroidal coordinates, the far-field velocity (i.e. uniaxial extensional flow) is

$$\mathbf{u}^\infty = \frac{c^2 b\tau}{h_\tau}P_2(\xi)\hat{\boldsymbol{\tau}} + \frac{c^2 b\xi}{h_\xi}P_2(\tau)\hat{\boldsymbol{\xi}}, \qquad (A\,28)$$

where $\hat{\boldsymbol{\tau}}$ and $\hat{\boldsymbol{\xi}}$ are unit vectors, P_n are Legendre polynomials, and b is the semi-minor axis length of the vesicle. The interfacial boundary conditions for velocity are:

(i) continuity of velocity across interface, $[[\boldsymbol{u}]] = 0$;
(ii) surface incompressibility, $\nabla_s \cdot \boldsymbol{u} = 0$;
(iii) no penetration, $\boldsymbol{u} \cdot \boldsymbol{n} = 0$.

Because the normal velocity on the interface is zero, we can show that the tangential velocity must also vanish due to surface incompressibility. (To prove this fact, see (A 27), coupled with the fact that the tangential velocity must be zero at the ends of the vesicle due to symmetry.) Thus, the *velocity on the interface is exactly zero, and we can treat the vesicle as if it were effectively rigid at steady state.* We define the disturbance velocity outside the vesicle to be $\boldsymbol{u}_D = \boldsymbol{u} - \boldsymbol{u}^\infty$, and we solve for this quantity through the multipole expansion introduced in §A.2 (see (A 12) and (A 13)). The system of equations for the spectral coefficients of $\boldsymbol{u}_D$ are as follows.
Radial disturbance velocity

$$-c\tau P_2(\xi) = \sum_{n=0}^{\infty} [\tfrac{1}{2}\xi c_n^{out} P_n(\xi)(Q_n(\tau) - \tau Q_n'(\tau)) - \tfrac{1}{2}d_n^{out} P_n(\xi)Q_n'(\tau)] \quad \text{at } \tau = \tau^*. \quad \text{(A 29)}$$

Polar disturbance velocity

$$c\xi P_2(\tau) = \sum_{n=0}^{\infty} [\tfrac{1}{2}\tau c_n^{out} Q_n(\tau)(\xi P_n'(\xi) - P_n(\xi)) + \tfrac{1}{2}d_n^{out} Q_n(\tau)P_n'(\xi)] \quad \text{at } \tau = \tau^*. \quad \text{(A 30)}$$

From examining these two expressions, it is clear that the only non-zero coefficients are d_0^{out}, d_2^{out}, and c_1^{out}. Solving the equations above yields

$$d_2^{out} = \frac{c(3\tau^{*2} - 1)}{3Q_2(\tau^*)}, \quad d_0^{out} = \frac{\tfrac{1}{2}d_2^{out} Q_2'(\tau^*) - c\tau^*}{Q_0'(\tau^*)}, \quad c_1^{out} = \frac{-3c\tau^* + \tfrac{3}{2}d_2^{out} Q_2'(\tau^*)}{Q_1(\tau^*) - \tau^* Q_1'(\tau^*)}.$$
$$\text{(A 31a–c)}$$

Now that we have determined the velocity field, let us calculate the surface tension via the tangential stress boundary condition: $[[\boldsymbol{t} \cdot \boldsymbol{T} \cdot \boldsymbol{n}]] = -\boldsymbol{t} \cdot \nabla_s \sigma$. The shear stress on the interface can be broken into two fields: $\boldsymbol{T} = \boldsymbol{T}_D + \boldsymbol{T}^\infty$, where $\boldsymbol{T}_D$ is the shear stress from the disturbance velocity field and $\boldsymbol{T}^\infty$ is the shear stress from the far-field velocity. Using the stress expressions in (A 17), the tangential stress due to the disturbance velocity is

$$\hat{\boldsymbol{\tau}} \cdot \boldsymbol{T}_D \cdot \hat{\boldsymbol{\xi}} = -\sum_{n=0}^{\infty} (c_n^{out} c\tau\xi + cd_n^{out}) L_{\tau\xi}[Q_n(\tau)P_n(\xi)]$$
$$= \frac{\sqrt{\tau^2 - 1}\sqrt{1 - \xi^2}\xi}{c(\tau^2 - \xi^2)}[3c\tau + c_1^{out}(Q_1(\tau) - \tau Q_1'(\tau))] \quad \text{at } \tau = \tau^*. \quad \text{(A 32)}$$

Similarly, the tangential stress due to the far-field velocity is

$$\hat{\boldsymbol{\tau}} \cdot \boldsymbol{T}^\infty \cdot \hat{\boldsymbol{\xi}} = \hat{\boldsymbol{\tau}} \cdot (\nabla \boldsymbol{u}^\infty + \nabla \boldsymbol{u}^{\infty,T}) \cdot \hat{\boldsymbol{\xi}}$$
$$= -\frac{3\xi\tau \sqrt{1 - \xi^2}\sqrt{\tau^2 - 1}}{\tau^2 - \xi^2} \quad \text{at } \tau = \tau^*. \quad \text{(A 33)}$$

Invoking the tangential stress boundary condition, we now solve for the surface tension on the interface, which yields

$$\left.\begin{array}{l} \dfrac{\partial \sigma^{(0)}}{\partial \xi} = -h_\xi (\hat{\boldsymbol{\tau}} \cdot \boldsymbol{T} \cdot \hat{\boldsymbol{\xi}}) \\[10pt] \sigma^{(0)} = -\sqrt{\tau^2 - \xi^2}\sqrt{\tau^2 - 1}\, c_1^{out} b \left(Q_1(\tau) - \tau Q_1'(\tau) \right) \quad \text{at } \tau = \tau^*. \end{array}\right\} \tag{A 34}$$

As a consistency check, we confirm that this surface tension distribution satisfies the normal stress boundary condition with no bending force: $[[p]] + 2\sigma H = 0$, where $[[p]]$ is the viscous pressure jump across the interface, and $2\sigma H$ is the capillary pressure. We first calculate the mean curvature of the interface, which for a prolate spheroid is

$$H = \frac{\tau}{2cb(\tau^2 - \xi^2)^{3/2}} \left[\sqrt{\tau^2 - 1} + \frac{\tau^2 - \xi^2}{\sqrt{\tau^2 - 1}} \right] \quad \text{at } \tau = \tau^*. \tag{A 35}$$

We then calculate the viscous pressure on the interface using the multipole solution described in (A 14):

$$\begin{aligned} p_{out} &= -\frac{1}{c(\tau^2 - \xi^2)} \sum_{n=0}^{\infty} c_n^{out}[\xi(\tau^2 - 1)Q_n'(\tau)P_n(\xi) + \tau(1 - \xi^2)Q_n(\tau)P_n'(\xi)] \\ &= -\frac{c_1^{out}}{c}(\tau Q_1(\tau) - (\tau^2 - 1)Q_1'(\tau)) \\ &\quad + \frac{\tau(\tau^2 - 1)}{c(\tau^2 - \xi^2)} c_1^{out}(Q_1(\tau) - \tau Q_1'(\tau)) \quad \text{at } \tau = \tau^*. \end{aligned} \tag{A 36}$$

The pressure inside the vesicle is $p_{in} = p_{out} + 2\sigma H$. Solving for this quantity yields $p_{in} = -(2\tau^*/c)c_1^{out}(Q_1(\tau^*) - \tau^* Q_1'(\tau^*)) - (1/c)c_1^{out}Q_1'(\tau^*)$, which is a constant. The velocity, surface tension, and pressure fields are consistent with all boundary conditions, and thus a prolate ellipsoid is the shape of the vesicle in the limit of no bending forces ($Ca \to \infty$).

A.5. *Scaling arguments: asymmetric mode instability and pearling instability*

In §4, we state that the critical capillary numbers for the asymmetric instability and pearling instability obey the scaling law $Ca_c' = C \ln(L/R)/(L/R)$, where L is the vesicle length, R the radius and C is an $O(1)$ constant. We estimate the constants for these two transitions by approximating the vesicle as a cylinder in uniaxial extensional flow. For the asymmetric mode, we let the cylinder be at steady state, while for the pearling mode, we let the cylinder's radius decrease in time, as the vesicle's neck continuously thins before instability. We derive the constants for the two cases below.

A.5.1. *Asymmetric instability*

Because the vesicle is at steady-state, the velocity on the particle is zero, and thus the flow field is the same as that around a rigid body. From slender body theory, the shear stress on the vesicle's interface is thus

$$T_{rz} = \frac{\mu_{out}\dot{\epsilon}z}{R\ln(L/R)}, \tag{A 37}$$

where z is the coordinate along the flow direction ($z = 0$ at the centre of the particle and $z = \pm L/2$ at the ends). The tangential stress boundary condition dictates that the

shear stresses on the interface balance the surface tension gradients: $d\sigma/dz = -T_{rz}$. If we assume no tension at the ends of the vesicle, the surface tension becomes

$$\sigma = \sigma_{cen}\left[1 - 4\left(\frac{z}{L}\right)^2\right]; \quad \sigma_{cen} = \frac{\mu_{out}\dot{\epsilon}L^2}{8R\ln(L/R)}. \tag{A 38}$$

We expect the vesicle to become unstable when the capillary forces overcome the bending resistance of the interface. For a cylindrical membrane, this inequality corresponds to $\sigma_{cen}/R > \kappa/(2R^3)$, where κ is the bending modulus of the membrane (see (2.4) for bending force expression). Noting that the capillary number defined by Kantsler *et al.* (2008*a*) is $Ca' = \mu_{out}\dot{\epsilon}LR^2/\kappa$, we obtain the critical condition:

$$Ca'_c > 4\frac{\ln(L/R)}{L/R}. \tag{A 39}$$

Thus, for the asymmetric instability, the constant for the scaling relation is $C = 4$.

A.5.2. *Pearling instability*

Before the pearling transition, the vesicle extends continuously in flow, creating a central neck whose radius decreases in time. In this section, we model the vesicle as a cylinder in uniaxial extensional flow, with its radius R decreasing at a rate $\dot{R}$. We will calculate the surface tension of this configuration, and determine the conditions under which the tension becomes larger than the critical condition $\sigma_c = 3\kappa/(2R^2)$.

Before we begin, let us perform some simple scaling analysis. We expect the extensional flow to induce a surface velocity u_z on the vesicle, which in turn creates a radial velocity $\dot{R}$ due to the membrane's incompressibility. The lubrication flow initiated by these velocities induces a pressure gradient that scales as

$$p/L \sim \lambda\mu_{out}\frac{u_z}{R^2}. \tag{A 40}$$

This pressure should balance the surface tension from the extensional flow (as determined by slender body theory):

$$\sigma/R \sim \frac{\mu_{out}\dot{\epsilon}L^2}{R^2\ln(L/R)}. \tag{A 41}$$

Balancing the two equations yields $u_z \sim \dot{\epsilon}L/(\lambda\ln(L/R))$. For viscosity ratios of order unity (which we consider here), the surface velocity u_z is smaller than the far-field velocity u_z^∞ by a factor of $\ln(L/R)$. For now, we neglect such logarithmic corrections and *treat the vesicle as essentially rigid* when we are solving for the fluid flow outside the vesicle.

The tangential stress boundary condition states that the jump in tangential stresses must balance the surface tension gradients: $-d\sigma/dz = T_{rz}^{out} - T_{rz}^{in}$. We obtain the outer stress from slender body theory on a rigid particle, which is the same expression as (A 37):

$$T_{rz}^{out} = \frac{\mu_{out}\dot{\epsilon}z}{R\ln(L/R)}. \tag{A 42}$$

The shear stress on the inner surface is determined by the flow inside the cylinder, which is governed by the lubrication equations. The z-velocity satisfies

$$\lambda\mu_{out}\frac{1}{r}\frac{\partial}{\partial r}\left(r\frac{\partial u_z}{\partial r}\right) = \frac{\partial p}{\partial z}, \quad p = p(z) \text{ only.} \tag{A 43}$$

The solution to this velocity field is

$$u_z = \frac{1}{4\lambda\mu_{out}} \frac{\partial p}{\partial z}(r^2 + C) = f(z)r^2 + g(z). \tag{A 44}$$

To determine f and g, we apply continuity of velocity and surface incompressibility. The integrated continuity equation is

$$R\dot{R} + \int_0^R \frac{\partial u_z}{\partial z} r \, dr = 0. \tag{A 45}$$

The surface incompressibility condition is $\partial u_z/\partial z = -u_r/r$ on the surface $r = R$. Applying these boundary conditions gives the velocity, pressure, and shear-stress fields on the interface:

$$u_z = -\frac{\dot{R}z}{R}, \quad p^{in} = \frac{4\mu\lambda\dot{R}z^2}{R^3}, \quad T_{rz}^{in} = \frac{4\mu\lambda\dot{R}z}{R^2}. \tag{A 46a–c}$$

Now that we have the shear stresses, we solve for the surface tension, assuming no tension at the ends of the cylinder. Substituting the stresses (A 42) and (A 46) into the tangential stress boundary condition $-d\sigma/dz = T_{rz}^{out} - T_{rz}^{in}$ yields

$$\sigma = \sigma_{cen}\left[1 - 4\left(\frac{z}{L}\right)^2\right], \quad \sigma_{cen} = \frac{\mu_{out}\dot{\epsilon}L^2}{8R\ln(L/R)} - \frac{\lambda\mu_{out}\dot{R}L^2}{2R^2}. \tag{A 47}$$

To determine the radial velocity of the interface $\dot{R}$, we invoke the normal stress boundary condition, which for a cylindrical geometry is

$$p^{in} + p_0 = \frac{\sigma}{R} - \frac{\kappa}{2R^3}. \tag{A 48}$$

In the above equation, κ is the bending modulus of the interface. We substitute the interior pressure p^{in} and the surface tension σ into the above balance, which yields two equations for the constant pressure p_0 and the deformation rate $\dot{R}$:

$$p_0 = \sigma_{cen} - \frac{\kappa}{2R^3}, \quad \dot{R} = -\frac{\dot{\epsilon}R}{4\lambda\ln(L/R)}. \tag{A 49a,b}$$

Now that we have the deformation rate $\dot{R}$, we substitute this expression into the surface tension (A 47) to obtain the final form for the tension at the centre of the particle:

$$\sigma_{cen} = \frac{\mu_{out}\dot{\epsilon}L^2}{4R\ln(L/R)}. \tag{A 50}$$

We expect a pearling instability to occur when this surface tension exceeds the critical condition $\sigma_c = 3\kappa/(2R^2)$. Noting that the capillary number defined by Kantsler *et al.* (2008a) is $Ca' = \mu_{out}\dot{\epsilon}LR^2/\kappa$, the stability criteria becomes

$$Ca'_c > 6\frac{\ln(L/R)}{L/R}. \tag{A 51}$$

Thus, for the pearling instability, the constant for the scaling relation is $C = 6$.

A.6. *Derivation of growth rates, pearling instability*

A.6.1. *Problem statement and scaling*

Suppose we have an infinitely long cylindrical vesicle of radius R that is initially at rest in a fluid of viscosity μ. The vesicle's membrane has a bending modulus κ and

an applied tension σ_0. Furthermore, the vesicle encloses a solution of viscosity $\lambda\mu$. If the interface experiences a small disturbance, under what conditions will we observe pearling?

Let us say that the membrane experiences a displacement:

$$r = R + b_k(t)e^{ikz}, \quad |b_k| \ll R, \tag{A 52}$$

where b_k represents a Fourier mode. This deformation creates a disturbance flow both inside and outside the vesicle, with the flow being linear in the radial velocity db_k/dt. The pressure from this flow balances the capillary and bending forces on the interface, leading to a dispersion relation. We derive the dispersion relation for each Fourier mode in this module.

For the rest of this section, we scale the radial and axial coordinates by the cylinder radius R, and all wavenumbers by $1/R$. We scale stresses by κ/R^3, and all surface tensions by κ/R^2. We scale time by the capillary time scale $t_c = \mu R^3/\kappa$, and all velocities by R/t_c. Lastly, we scale the membrane's deformation b_k by $|b_k|$. The non-dimensional radius of the cylinder is now:

$$r = 1 + \epsilon b_k e^{ikz}, \quad \epsilon \equiv \frac{|b_k|}{R} \ll 1 \tag{A 53}$$

where ϵ is the membrane strain, which we assume to be much smaller than unity. We further posit that the velocity, tension, and pressure fields follow a perturbation expansion in terms of ϵ as

$$\boldsymbol{u} = \epsilon \boldsymbol{u}^{(1)}, \quad \sigma = \sigma_0 + \epsilon \sigma^{(1)}, \quad p = p^{(0)} + \epsilon p^{(1)}. \tag{A 54a–c}$$

Under this assumption, the stress balances on the interface, to $O(\epsilon)$ are

$$\left. \begin{aligned} O(1) \text{ Normal stress: } & p_{in}^{(0)} = 2H^{(0)}\sigma^{(0)} + f_B^{(0)} \\ O(\epsilon) \text{ Normal stress: } & p_{in}^{(1)} - p_{out}^{(1)} = 2H^{(0)}\sigma^{(1)} + 2H^{(1)}\sigma_0 + f_B^{(1)} \\ O(\epsilon) \text{ Tangential stress: } & T_{rz,out}^{(1)} - T_{rz,in}^{(1)} = -\frac{d\sigma^{(1)}}{dz}. \end{aligned} \right\} \tag{A 55}$$

In the above expressions, terms with a superscript (1) are perturbed quantities that are linear in the deformation b_k of the interface. Terms with a superscript (0) are base-state quantities. We solve these balances in the following subsections.

A.6.2. *Differential geometry and base state*

For a cylindrical surface parameterized by (A 53), the principal curvatures on the interface to $O(\epsilon)$ are

$$\Upsilon_1 = \frac{1}{r} = 1 - \epsilon b_k \exp(ikz), \quad \Upsilon_2 = \epsilon b_k k^2 \exp(ikz). \tag{A 56a,b}$$

The mean and Gaussian curvatures are $H = 0.5(\Upsilon_1 + \Upsilon_2)$ and $K = \Upsilon_1\Upsilon_2$. The non-dimensional bending force is $f_B = 4KH - 4H^3 - 2\nabla_s^2 H$. Expressions for these quantities are thus,

$$H = \tfrac{1}{2} - \tfrac{1}{2}\epsilon b_k e^{ikz}(1 - k^2) \tag{A 57a}$$

$$f_B = -\tfrac{1}{2} + \epsilon b_k e^{ikz}(\tfrac{3}{2} - \tfrac{1}{2}k^2 + k^4). \tag{A 57b}$$

Substituting these expressions into the normal stress balance (A 55) yields for the $p_{in}^{(0)} = \sigma_0 - 1/2$ for the base state, which states that the equilibrium pressure inside the vesicle balances the applied tension plus the equilibrium bending force. For no applied tension, we recover the standard dimensional result $p_{in}^{(0)} = -\kappa/(2R^3)$. At $O(\epsilon)$, the normal stress balance simplifies to

$$p_{in}^{(1)} - p_{out}^{(1)} - \sigma^{(1)} = b_k e^{ikz}[(k^2 - 1)\sigma_0 + \tfrac{3}{2} - \tfrac{1}{2}k^2 + k^4]. \tag{A 58}$$

In the next section, we determine the perturbed tensions and pressures by solving the Stokes flow equations inside and outside the cylinder.

A.6.3. *Determine perturbation velocity, tension and pressure fields*

To calculate the perturbation stresses on the vesicle's membrane, we solve the full Stokes equations inside and outside the cylinder. Recall, the solution to Stokes equations is (Tran-Cong & Blake 1982; Dassios *et al.* 2004)

$$\boldsymbol{u} = \nabla(\boldsymbol{x} \cdot \boldsymbol{\Phi} + \chi) - 2\boldsymbol{\Phi}, \quad p = 2\eta\nabla \cdot \boldsymbol{\Phi}, \tag{A 59a,b}$$

where χ and $\boldsymbol{\Phi}$ are harmonic functions, and η is the non-dimensional viscosity of the medium (in our case, $\eta = 1$ outside the cylinder, and λ inside the cylinder). These equations automatically satisfy incompressibility: $\nabla \cdot \boldsymbol{u} = 0$. Because we decompose the surface deformation into Fourier modes (A 53), the appropriate choice of harmonic functions for a cylindrical geometry is

$$\left.\begin{array}{ll} \chi_{in} = A I_0(kr)e^{ikz}, & \boldsymbol{\Phi}_{in} = B I_1(kr)e^{ikz}\hat{\boldsymbol{r}} \\ \chi_{out} = E K_0(kr)e^{ikz}, & \boldsymbol{\Phi}_{out} = F K_1(kr)e^{ikz}\hat{\boldsymbol{r}} \end{array}\right\} \tag{A 60}$$

where A, B, E and F are undetermined constants, and I_0, I_1, K_0 and K_1 are modified Bessel functions. Here $I_0(x)$ and $I_1(x)$ are finite at the origin, while $K_0(x)$ and $K_1(x)$ decay at infinity. We will use the following Bessel function identities to simplify our algebra:

$$\left.\begin{array}{ll} I_0'(x) = I_1(x), & (xI_1(x))' = xI_0(x) \\ K_0'(x) = -K_1(x), & (xK_1(x))' = -xK_0(x). \end{array}\right\} \tag{A 61}$$

When we substitute our chosen harmonic functions into equations (A 59), we obtain the following velocity and pressure fields inside and outside the cylinder.

(i) Inside cylinder ($r < 1$)

$$\left.\begin{array}{l} u_r = e^{ikz}[AkI_1(kr) + BkrI_0(kr) - 2BI_1(kr)] \\ u_z = -ie^{ikz}[-AkI_0(kr) - BkrI_1(kr)] \\ p = e^{ikz}[2B\lambda kI_0(kr)]. \end{array}\right\} \tag{A 62}$$

(ii) Outside cylinder ($r > 1$)

$$\left.\begin{array}{l} u_r = e^{ikz}[-EkK_1(kr) - FkrK_0(kr) - 2FK_1(kr)] \\ u_z = -ie^{ikz}[-EkK_0(kr) - FkrK_1(kr)] \\ p = e^{ikz}[-2FkK_0(kr)]. \end{array}\right\} \tag{A 63}$$

We solve for the undetermined coefficients A, B, E and F by applying the kinematic boundary condition and surface incompressibility boundary condition. The kinematic boundary condition states that the interface expands and contracts with the radial velocity $u_r = \dot{b}_k e^{ikz}$. Surface incompressibility states that $(\delta_{ij} - n_i n_j)(\partial u_i/\partial x_j) = 0$ on the interface, which implies $\partial u_z/\partial z = -u_r$ on $r = 1$. Applying these boundary conditions to both flows yields the solutions

$$
\left.\begin{aligned}
A &= \dot{b}_k \alpha^{-1}(I_1 k^2 - I_0 k + 2I_1) \\
B &= \dot{b}_k \alpha^{-1}(I_1 k - I_0 k^2) \\
\alpha &= k(I_1^2 k^2 - I_0^2 k^2 + 2I_0 I_1 k)
\end{aligned}\right\} \tag{A 64}
$$

$$
\left.\begin{aligned}
E &= \dot{b}_k \beta^{-1}(-K_1 k^2 - K_0 k - 2K_1) \\
F &= \dot{b}_k \beta^{-1}(K_1 k + K_0 k^2) \\
\beta &= k(K_1^2 k^2 - K_0^2 k^2 - 2K_0 K_1 k).
\end{aligned}\right\} \tag{A 65}
$$

In the above solutions, all Bessel functions are evaluated at the wavenumber k. Now that we have the disturbance velocity and pressure fields, let us calculate the pressure jump across the interface $r = 1$:

$$
p_{in}^{(1)} - p_{out}^{(1)} = e^{ikz}[2B\lambda k I_0 + 2Fk K_0]. \tag{A 66}
$$

Similarly, we can calculate the perturbed surface tension, if we note that for each Fourier mode, $-ik\sigma^{(1)} = [[T_{rz}^{(1)}]]$, where $T_{rz}^{(1)}$ is the shear stress (which is equal to $T_{rz}^{(1)} = \eta((\partial u_z/\partial r) + (\partial u_r/\partial z))$ for a Newtonian fluid). Thus, the surface tension is

$$
\sigma^{(1)} = e^{ikz}[2Ek K_1 + 2F(kK_0 + K_1) + 2\lambda A k I_1 + 2\lambda B(k I_0 - I_1)]. \tag{A 67}
$$

A.6.4. *Dispersion relationship*

We substitute the pressure and surface tension expressions in (A 66) and (A 67) into the normal stress balance in (A 58). This operation yields a dispersion relationship for the Fourier mode b_k. If we define the perturbation growth rate s as the ratio of the deformation rate $\dot{b}_k$ to the deformation b_k, our dispersion relationship is

$$
\begin{aligned}
s(k) &\equiv \frac{\dot{b}_k}{b_k} = \frac{\Omega(k)}{\Lambda(k)}, \\
\Omega(k) &= (k^2 - 1)\sigma_0 + \tfrac{3}{2} - \tfrac{1}{2}k^2 + k^4, \\
\Lambda(k) &= 2k(k^2 + 1)[\beta^{-1}K_1^2 - \lambda\alpha^{-1}I_1^2].
\end{aligned} \tag{A 68}
$$

The numerator $\Omega(k)$ are contributions from bending and curvature forces, while the denominator $\Lambda(k)$ is purely from hydrodynamic stresses on the interface. The expressions for α and β are in (A 64) and (A 65).

It turns out that the hydrodynamical factor $\Lambda(k)$ is negative for all wavenumbers k. Thus, the only way to have an instability is to have the bending and curvature contribution $\Omega(k)$ be less than zero. If the applied tension $\sigma_0 > 3/2$, we are guaranteed a long-wavelength instability in $0 < k < 1$. This is the *pearling instability* that we are attempting to describe. If $\sigma_0 < -4.328$, we are guaranteed an instability for $k > 1$. This instability is the *buckling/wrinkling* instability, as it creates short-wavelength ripples on the surface due to the creation of negative tensions. These stability margins agree with all previous studies, as we obtain the same bending factor $\Omega(k)$ (Goldstein *et al.* 1996; Powers 2010; Boedec *et al.* 2014). Our hydrodynamical factor $\Lambda(k)$ agrees with

Boedec *et al.* (2014), which gives the most accurate dispersion relationship for the pearling phenomenon. Previous studies computed $\Lambda(k)$ slightly incorrectly, as they forgot to take into account the spatially varying tension (i.e. $\sigma^{(1)}$) in their derivations (Goldstein *et al.* 1996; Powers 2010).

REFERENCES

ABKARIAN, M. & VIALLAT, A. 2008 Vesicles and red blood cells in shear flow. *Soft Matt.* **4**, 653–657.

ABRAMOWITZ, M. & STEGUN, I. A. 1972 *Handbook of Mathematical Functions with Formulas, Graphs, and Mathematical Tables*. National Bureau of Standards.

ABREU, D. & SEIFERT, U. 2013 Noisy nonlinear dynamics of vesicles in flow. *Phys. Rev. Lett.* **110**, 238103.

ALBERTS, B., BRAY, D., HOPKIN, K., JOHNSON, A., LEWIS, J., RAFF, M., ROBERTS, K. & WALTERS, P. 2004 *Essential Cell Biology*, 2nd edn. Garland Science.

ANTONIETTI, M. & FORSTER, S. 2003 Vesicles and liposomes: a self-assembly principle beyond lipids. *Adv. Mater.* **15**, 1323–1333.

BATCHELOR, G. K. 1970 Slender-body theory for particles of arbitrary cross-section in Stokes flow. *J. Fluid Mech.* **44**, 419–440.

BENTLEY, B. J. & LEAL, L. G. 1986 An experimental investigation of drop deformation and breakup in steady two-dimensional linear flows. *J. Fluid Mech.* **167**, 241–283.

BLAWZDZIEWICZ, J., CRISTINI, V. & LOEWENBERG, M. 1999 Stokes flow in the presence of a planar interface covered with incompressible surfactant. *Phys. Fluids* **11**, 251–258.

BOEDEC, G., JAEGER, M. & LEONETTI, M. 2012 Settling of a vesicle in the limit of quasispherical shapes. *J. Fluid Mech.* **690**, 227–261.

BOEDEC, G., JAEGER, M. & LEONETTI, M. 2014 Pearling instability of a cylindrical vesicle. *J. Fluid Mech.* **743**, 262–279.

BOYD, S. P. & VANDENBERGHE, L. 2004 *Convex Optimization*. Cambridge University Press.

CALLENS, N., MINETTI, C., COUPIER, G., MADER, M., DUBOIS, F., MISBAH, C. & PODGORSKI, P. 2008 Hydrodynmamic lift of vesicles under shear flow in microgravity. *Europhys. Lett.* **83**, 24002.

DASSIOS, G., PAYATAKES, A. C. & VAFEAS, P. 2004 Interrelation between Papkovich–Neuber and Stokes general solutions of the stokes equations in spheroidal geometry. *Q. J. Mech. Appl. Maths* **57**, 181–203.

DE GENNES, P. G. 1974 Coil-stretch transition of dilute flexible polymers under ultrahigh velocity gradients. *J. Chem. Phys.* **60**, 5030–5042.

DECHAMPS, J., KANTSLER, V. & STEINBERG, V. 2009 Phase diagram of single vesicle dynamical states in shear flow. *Phys. Rev. Lett.* **102**, 118105.

GIRES, P. Y., DANKER, G. & MISBAH, C. 2012 Hydrodynamic interaction between two vesicles in a linear shear flow: asymptotic study. *Phys. Rev.* E **86**, 011408.

GOLDSTEIN, R. E., NELSON, P., POWERS, T. R. & SEIFERT, U. 1996 Front propagation in the pearling instability of tubular vesicles. *J. Phys. II France* **6**, 767–796.

HELFRICH, W. 1973 Elastic properties of lipid bilayers: theory and possible experiments. *Z. Naturforsch.* C **28**, 693–703.

HOBSON, E. W. 1931 *The Theory of Spherical and Ellipsoidal Harmonics*. Cambridge University Press.

HU, Y. T., PINE, D. J. & LEAL, L. G. 2000 Drop deformation, breakup, and coalescence with compatibilizer. *Phys. Fluids* **12**, 484–489.

HUANG, H. L., ABKARIAN, M. & VIALLAT, A. 2011 Sedimentation of vesicles: from pear-like shapes to microtether extrusion. *New J. Phys.* **13**, 035026.

IMMORDINO, M. L., DOSIO, F. & CATTEL, L. 2006 Stealth liposomes: review of the basic science, rationale, and clinical applications, existing and potential. *Intl J. Nanomed.* **3**, 297–315.

JANSSEN, J. J. M., BOON, A. & AGTEROF, M. W. G. 1997 Influence of dynamic interfacial properties on droplet breakup in plane hyperbolic flow. *AIChE J.* **43**, 1436–1447.

KANTSLER, V., SEGRE, E. & STEINBERG, V. 2008a Critical dynamics of vesicle stretching transition in elongational flow. *Phys. Rev. Lett.* **101**, 048101.

KANTSLER, V., SEGRE, E. & STEINBERG, V. 2008b Dynamics of interacting vesicles and rheology of vesicle suspension in shear flow. *Europhys. Lett.* **82**, 58005.

LEAL, L. G. 2007 *Advanced Transport Phenomena: Fluid Mechanics and Convective Transport Processes*. Cambridge University Press.

LEVANT, M., DESCHAMPS, J., AFIK, E. & STEINBERG, V. 2012 Characteristic spatial scale of vesicle pair interactions in a plane linear flow. *Phys. Rev.* E **85**, 056306.

LEVANT, M. & STEINBERG, V. 2012 Amplification of thermal noise by vesicle dynamics. *Phys. Rev. Lett.* **109**, 268103.

MADER, M., VITKOVA, V., ABKARIAN, M., VIALLAT, A. & PODGORSKI, T. 2006 Dynamics of viscous vesicles in shear flow. *Eur. Phys. J.* E **19**, 389–397.

MEDINA, O. P., ZHU, Y. & KAIREMO, K. 2004 Targeted liposomal drug delivery in cancer. *Curr. Pharm. Des.* **24**, 2981–2989.

NOIREAUX, V. & LIBCHABER, A. 2004 A vesicle bioreactor as a step toward an artificial cell assembly. *Proc. Natl Acad. Sci. U.S.A.* **101**, 17669–17674.

PAN, J., TRISTRAM-NAGLE, S., KUCERKA, N. & NAGLE, J. F. 2008 Temperature dependence of structure, bending rigidity, and bilayer interactions of dioleoylphosphatidylcholine bilayers. *Biophys. J.* **94**, 117–124.

PODGORSKI, T., CALLENS, N., MINETTI, C., COUPIER, G. & MISBAH, C. 2011 Dynamics of vesicle suspensions in shear flow between walls. *Microgravity Sci. Technol.* **23**, 263–270.

POWERS, T. R. 2010 Dynamics of filaments and membranes in a viscous fluid. *Rev. Mod. Phys.* **82**, 1607–1631.

POZRIKIDIS, C. 1992 *Boundary Integral and Singularity Methods for Linearized Viscous Flow*. Cambridge University Press.

RALLISON, J. M. 1984 The deformation of small viscous drops and bubbles in shear flows. *Annu. Rev. Fluid Mech.* **16**, 45–66.

RAWICZ, W., OLBRICH, K. C., MCINTOSH, T., NEEDHAM, D. & EVANS, E. 2000 Effect of chain length and unsaturation on elasticity of lipid bilayers. *Biophys. J.* **79**, 328–339.

SEIFERT, U. 1997 Configurations of fluid membranes and vesicles. *Adv. Phys.* **46**, 13–137.

SEIFERT, U., BERNDL, K. & LIPOWSKY, R. 1991 Shape transformations of vesicles: phase diagram for spontaneous curvature and bilayer-coupling models. *Phys. Rev.* A **44**, 1182–1202.

SHARMA, A. & SHARMA, U. S. 1997 Liposomes in drug delivery: progress and limitations. *Intl J. Pharm.* **154**, 123–140.

SPANN, A. P. 2013 Loop subdivision surface boundary integral simulations for vesicles in shear and extensional flows. PhD thesis, Stanford University.

SPANN, A. P., ZHAO, H. & SHAQFEH, E. S. G. 2014 Loop subdivision surface boundary integral method simulations of vesicles at low reduced volume ratio in shear and extensional flow. *Phys. Fluids* **26**, 031902.

SPJUT, J. E. 2010 Trapping, deformation, and dynamics of phospholipid vesicles. MS thesis, University of California, Berkeley. Chap. 3.

STONE, H. A. 1994 Dynamics of drop deformation and breakup in viscous fluids. *Annu. Rev. Fluid Mech.* **26**, 65–102.

STONE, H. A., BENTLEY, B. J. & LEAL, L. G. 1986 An experimental study of transient effects in the breakup of viscous drops. *J. Fluid Mech.* **173**, 131–158.

TIMMERMANS, M. L. E. & LISTER, J. R. 2002 The effect of surfactant on the stability of a liquid thread. *J. Fluid Mech.* **459**, 289–306.

TOMOTIKA, S. 1935 On the instability of a cylindrical thread of a viscous liquid surrounded by another viscous fluid. *Proc. R. Soc. Lond.* A **150**, 332–337.

TRAN-CONG, T. & BLAKE, J. R. 1982 General solution of the Stokes' flow equations. *J. Math. Anal. Appl.* **90**, 72–84.

VEERAPANENI, S. K., GUEYFFIER, D., BIROS, G. & ZORIN, D. 2009 A numerical method for simulating the dynamics of 3D axisymmetric vesicles suspended in viscous flows. *J. Comput. Phys.* **228**, 7233–7249.

VITKOVA, V., MADER, M., POLACK, B., MISBAH, C. & PODGORSKI, T. 2008 Micro-macro link in rheology of erythrocyte and vesicle suspensions. *Biophys. J.* **95**, L33–L35.

VLAHOVSKA, P. M. & GRACIA, R. S. 2007 Dynamics of a viscous vesicle in linear flows. *Phys. Rev.* E **75**, 016313.

VLAHOVSKA, P. M., PODGORSKI, T. & MISBAH, C. 2009 Vesicles and red blood cells in flow: from individual dynamics to rheology. *C. R. Phys.* **10**, 775–789.

ZABUSKY, N. J., SEGRE, E., DESCHAMPS, J., KANTSLER, V. & STEINBERG, V. 2011 Dynamics of vesicles in shear and rotational flows: modal dynamics and phase diagram. *Phys. Fluids* **23**, 041905.

ZHANG, J., ZAHN, J. D., TAN, W. & LIN, H. 2013 A transient solution for vesicle electrodeformation and relaxation. *Phys. Fluids* **25**, 071903.

ZHAO, H. & SHAQFEH, E. S. G. 2011 The dynamics of a vesicle in simple shear flow. *J. Fluid Mech.* **674**, 578–604.

ZHAO, H. & SHAQFEH, E. S. G. 2013a The dynamics of a non-dilute vesicle suspension in a simple shear flow. *J. Fluid Mech.* **725**, 709–731.

ZHAO, H. & SHAQFEH, E. S. G. 2013b The shape stability of a lipid vesicle in a uniaxial extensional flow. *J. Fluid Mech.* **719**, 345–361.

ZHAO, H., SPANN, A. P. & SHAQFEH, E. S. G. 2011 The dynamics of a vesicle in a wall-bound shear flow. *Phys. Fluids* **23**, 121901.

ZHONG-CAN, O. Y. & HELFRICH, W. 1989 Bending energy of vesicle membranes: general expressions for the first, second, and third variation of the shape energy and applications to spheres and cylinders. *Phys. Rev.* A **39**, 5280–5288.